Observation of eccentric binary black hole mergers with second and third generation gravitational wave detector networks

Zhuo Chen, E. A. Huerta, Joseph Adamo, Roland Haas, Eamonn O'Shea, Prayush Kumar, and Chris Moore

Observation of eccentric binary black hole mergers with second and third generation gravitational wave detector networks

Zhuo Chen,[1, 2] E. A. Huerta,[1, 2, 3] Joseph Adamo,[1, 2] Roland Haas,[1] Eamonn O'Shea,[4] Prayush Kumar,[5, 4] and Chris Moore[6]

[1] National Center for Supercomputing Applications, University of Illinois at Urbana-Champaign, Urbana, Illinois 61801, USA
[2] Department of Physics, University of Illinois at Urbana-Champaign, Urbana, Illinois 61801, USA
[3] Department of Astronomy, University of Illinois at Urbana-Champaign, Urbana, Illinois 61801, USA
[4] Cornell Center for Astrophysics and Planetary Science, Cornell University, Ithaca, New York 14853, USA
[5] International Centre for Theoretical Sciences, Tata Institute of Fundamental Research, Bangalore 560012, India
[6] University of Birmingham, Birmingham B15 2TT, United Kingdom

We introduce an improved version of the Eccentric, Non-spinning, Inspiral-Gaussian-process Merger Approximant (`ENIGMA`) waveform model that utilizes a more stable and robust numerical method to smoothly connect the analytical relativity-based inspiral evolution with the numerical relativity-based merger phase. We find that this ready-to-use model can: (i) produce physically consistent signals, without reporting any failures, when sampling over 1M samples that were randomly chosen over the $m_{\{1, 2\}} \in [5\mathrm{M}_\odot, 50\mathrm{M}_\odot]$ parameter space, and the entire range of binary inclination angles; (ii) produce waveforms within 0.04 seconds, averaged over 1000 iterations, from an initial gravitational wave frequency $f_{\mathrm{GW}} = 15\,\mathrm{Hz}$ and at a sample rate of 8192 Hz; and (iii) reproduce the physics of quasi-circular mergers, since its overlap with `SEOBNRv4` waveforms is $\mathcal{O} \geq 0.99$ assuming advanced LIGO zero detuned high power noise configuration, and signals generated from $f_{\mathrm{GW}} = 15\,\mathrm{Hz}$. We utilize `ENIGMA` to compute the expected signal-to-noise ratio (SNR) distributions of eccentric binary black hole mergers assuming the existence of second and third generation gravitational wave detector networks. For second generation detectors, we assume the geographical location and detection sensitivities of the twin LIGO detectors, Virgo, KAGRA, LIGO-India, and a LIGO-type detector in Australia. For third generation detectors, we assume the geographical location of second generation detectors, and use the proposed sensitivities of the Cosmic Explorer and the Einstein Telescope. In the context of advanced LIGO-type detectors, we find that the SNR of eccentric mergers is always larger than quasi-circular mergers for systems with $e_0 \leq 0.4$ at $f_{\mathrm{GW}} = 10\,\mathrm{Hz}$, even if the timespan of eccentric signals is just a third of quasi-circular systems with identical total mass and mass-ratio. For Cosmic Explorer-type detector networks, we find that eccentric mergers have similar SNRs than quasi-circular systems for $e_0 \leq 0.3$ at $f_{\mathrm{GW}} = 10\,\mathrm{Hz}$. Systems with $e_0 \sim 0.5$ at $f_{\mathrm{GW}} = 10\,\mathrm{Hz}$ have SNRs that range between 50%-90% of the SNR produced by quasi-circular mergers, even if these eccentric signals are just between a third to a tenth the length of quasi-circular systems. For Einstein Telescope-type detectors, we find that eccentric mergers have similar SNRs than quasi-circular systems for $e_0 \leq 0.4$ at $f_{\mathrm{GW}} = 5\,\mathrm{Hz}$. The most eccentric events in our sample, $e_0 \sim 0.6$ at $f_{\mathrm{GW}} = 5\,\mathrm{Hz}$, merge at least five times faster than quasi-circular systems, and may be detectable with SNRs between 50%-85% the SNR of quasi-circular mergers with identical binary components.

I. INTRODUCTION

The gravitational wave (GW) detection of binary black hole (BBH) mergers with the advanced LIGO [1, 2] and advanced Virgo [3] detectors is now a common occurrence [4–6]. As these detectors gradually reach their target sensitivity, and more detectors join the existing GW detector network, it is expected that an ever increasing number of GW observations will enable statistical analyses that may shed new and detailed information about the astrophysical origin of compact binary sources [7–10]. In this paper we are particularly interested in BBHs formed in dense stellar environments, such as core-collapsed globular clusters or galactic nuclei, and are expected to enter the frequency band of ground-based GW detectors with non-negligible eccentricity [11–50]. Recent studies suggest that the expected detection rate of eccentric BBH mergers for second generation detectors is about 100 mergers per cubic Gpc per year [51], and about 1700 mergers per cubic Gpc per year for binary neutron star mergers [52]. For third generation detectors, it may be possible to observe from several hundred to a few thousand eccentric mergers per cubic Gpc per year [28, 53].

The study and modeling of eccentric BBH systems has gained traction in recent years. Waveform models that describe the GW emission of these sources has rapidly evolved from inspiral-only GW models [28, 45, 54–61], to semi-analytical and machine-learning based models that describe the inspiral-merger-ringdown evolution of these GW sources [62–68]. Numerical relativity has also been used to obtain insights into the non-linear dynamics of these systems throughout merger and ringdown [69–73], and to study the impact of higher-order waveform modes for the detection of eccentric BBH mergers [74]. Recent studies have also shed light on how to extract signatures of dynamical formation in GW sources detected by advanced LIGO and Virgo [51, 75–78], estimate the eccentricity of GW signals [53], including the recent detection GW190425 [79].

In this article we introduce an improved version of the inspiral-merger-ringdown ENIGMA waveform model [62], which describes the GW emission of non-spinning BHs that evolve on moderately eccentric orbits, to compare the signal-to-noise (SNR) distribution of quasi-circular and moderately eccentric BBH mergers. This study is motivated by a number of observations, e.g., it has been documented in the literature that GWs emitted by BBHs that evolve on moderately eccentric orbits exhibit the following properties [69]: (i) the waveform amplitude of eccentric signals tends to be larger than that of quasi-circular ones during the early inspiral evolution; (ii) GWs produced by eccentric BBH mergers are shorter than those of quasi-circular BBH mergers. In view of these observations, one may naturally like to explore the astrophysical scenarios in which eccentric and quasi-circular BBH mergers have similar SNR distributions, and to quantify the eccentricity threshold at which condition (i) above no longer compensates for condition (ii) leading to BBH mergers that produce GWs whose SNRs are lower than quasi-circular ones. This article aims to shed light on these points in the context of second and third generation, ground-based GW detector networks.

The rest of this article is organized as follows. Section II provides a brief description of the new features in the ENIGMA waveform model [62], and a number of benchmark analyses we have conducted to thoroughly test it. Section III introduces data analysis tools that we use throughout this article. In Section IV we describe the second and third generation GW detector networks considered in this study, including the power spectral densities (PDSs) used to represent each GW detector. We present and discuss our results in Sections IV A and IV B. We summarize our findings and future work in Section V.

II. ENIGMA WAVEFORM MODEL

The ENIGMA model has two pieces. The first combines post-Newtonian (PN) results that describe the dynamics of moderately eccentric BBH mergers, and encompasses instantaneous, tails and tails-of-tails contributions, and a contribution due to non-linear memory [62, 80–82]. This framework is equivalent to the PN approximant TaylorT4 at 3PN order in the zero eccentricity limit. ENIGMA also incorporates higher-order PN corrections for the energy flux of quasi-circular binaries and gravitational self-force corrections to the binding energy of compact binaries up to 6PN order. The equations of motion that describe the orbital dynamics and the radiative evolution of the system are expressed in terms of the gauge-invariant quantity $x = (M\omega)^{2/3}$, where M represents the total mass of the binary and ω is the mean orbital frequency. We use this parametrization because it provides an accurate description of eccentric BBH mergers when directly compared to numerical relativity simulations [54, 62, 83].

The second part of the ENIGMA model is a stand-alone merger waveform. Since ENIGMA is constructed under the assumption that moderately eccentric compact binaries circularize before merger, this part of the model is designed to describe the late inspiral-merger-ringdown of quasi-circular BBHs. The merger part is constructed using Gaussian process emulation [84], i.e., we train a machine learning algorithm to do interpolation using a dataset of numerical relativity waveforms that describe non-spinning BHs on quasi-circular orbits [85]. Once trained, this Gaussian emulator produces merger waveforms within milliseconds. We then conduct an optimization procedure to identify the optimal time at which we can smoothly connect the inspiral and merger pieces of the waveform model. The inclusion of higher-order post-Newtonian and self-force corrections improves the modeling of the inspiral phase, facilitating its attachment to the merger waveform during the late-time inspiral evolution. We fine-tune this late-time attachment condition by maximizing the overlap, computed using advanced LIGO zero detuned high power configuration and a minimum filtering frequency of 15Hz, between quasi-circular ENIGMA waveforms and SEOBNRv4 waveforms [86]. By construction, the higher-order PN and self-force results we use to model the inspiral evolution of ENIGMA are reliable for eccentricities $e_0 \leq 0.6$—see the analytical expressions used for this purpose in Appendix A of [63]. Furthermore, since we also assume that the binary systems circularize prior to attaching the quasi-circular merger waveform, the waveform approximant will only attach a merger waveform is the residual eccentricity prior to merger is ≤ 0.01. If this condition is not met, then the approximant will output an error stating that the residual eccentricity is too large to attach a quasi-circular merger waveform.

New features of the ENIGMA model The two key improvements to ENIGMA are in the merger attachment and the handling of the binary inclination angle.

For the merger attachment, we sample the range $M\omega \in [0.02, 0.1]$ in steps of 1×10^{-4}, and for each frequency value, $M\omega_i$, we construct a complete ENIGMA waveform whose merger phase is attached at $M\omega_i$. Each of these waveforms is then compared with an SEOBNRv4 waveform that describes the same binary system, densely covering the parameter space $m_{\{1, 2\}} \in [5\mathrm{M}_\odot, 50\mathrm{M}_\odot]$.

For this calibration procedure, we use standard tools, namely, if h and s denote ENIGMA and SEOBNRv4 waveforms, $S_n(f)$ the power spectral density (PSD) of a given GW detector, and $\tilde{h}(f)$ the Fourier transform of $h(t)$, the noise-weighted inner product between h and s is given by

$$(h|s) = 2 \int_{f_0}^{f_1} \frac{\tilde{h}^*(f)\tilde{s}(f) + \tilde{h}(f)\tilde{s}^*(f)}{S_n(f)} \mathrm{d}f. \qquad (1)$$

For calibration purposes, we set the initial GW frequency to $f_0 = f_{\mathrm{GW}} = 15\,\mathrm{Hz}$, and use the zero detuned high power noise curve for advanced LIGO [87] with $f_1 = 4096\,\mathrm{Hz}$. The waveforms are produced at a sample rate of $8192\,\mathrm{Hz}$. The overlap between h and s is defined as

$$\mathcal{O}(h,\,s) = \max_{t_c\,\phi_c}\left(\hat{h}|\hat{s}_{[t_c,\,\phi_c]}\right) \quad \text{with} \qquad (2)$$

$$\hat{h} = h\,(h|h)^{-1/2}\,, \qquad (3)$$

where $\hat{s}_{[t_c,\,\phi_c]}$ indicate that the normalized waveform $\hat{s}$ has been time- and phase-shifted. We then determine the attachment frequency value $M\omega^*$ that maximizes the overlap between the two aforementioned waveform families across the parameter space under consideration, and use it to compute the exact attachment time t_{attach}. The previous description summarizes the method utilized to calibrate ENIGMA in [62]. However, one realizes that this procedure only tells us that when the orbital frequency during inspiral meets the condition $\omega_{\text{inspiral}} > \omega^*$ then we know that t_{attach} lies within the range $[t - dt, t]$. Thus, our accuracy is dependent on the size of dt, which for values we have used to describe binary black hole mergers, i.e., $dt = \{1/4096s, 1/8192s\}$, dt may be inaccurate. To address this limitation and better compute t_{attach}, we have implemented the bisection root finding method on the range $[t - dt, dt]$ to determine the exact value of t_{attach}. After this addition, we have tested and found that t_{attach} so obtained is sufficiently accurate up to the limit of floating point precision. Figure 1 shows the difference between the two methodologies used to construct complete ENIGMA waveforms.

Using the aforementioned approach to produce complete ENIGMA waveforms, Figure 2 presents the overlap between our newly recalibrated ENIGMA model in the quasi-circular limit and SEOBNRv4 waveforms. It is worth pointing out that when we tested waveform production at scale, we found that we can randomly sample the parameter space shown in Figure 2, and produce 1M waveforms error free. In contrast, about 1% of these waveforms would not be produced with the previous version of ENIGMA due to instabilities in the merger attachment routine.

The second improvement to ENIGMA is the handling of the binary inclination angle. In the original version of ENIGMA, the calibration was conducted assuming zero inclination. We relax that assumption in this study. While for quasi-circular mergers the inclination angle enters the amplitude of the plus and cross polarizations as a trivial multiplicative factor, the inclination angle modifies the amplitude of the plus and cross polarizations in a non-trivial fashion even at the leading-order PN correction level, as shown in Eqs. (8) and (9) in [63]. In this version of ENIGMA we now provide a robust handling of the inclination angle when smoothly connecting the inspiral and merger waveforms. To get a glimpse of the importance of the inclination angle in the morphology of eccentric mergers, Figure 3 presents the real part of the waveform strain that describes a BBH merger with $e_0 = 0.3$ at $f_{\text{GW}} = 9\,\text{Hz}$, mass-ratio $q = 3$ and total mass $M = 60\text{M}_\odot$.

Figure 3 shows that in stark contrast with quasi-circular mergers, changing the inclination angle from $i = 0$ to $i = \pi/2$ does not lead to a simple reduction of the waveform amplitude by an overall factor of $1/2$. Rather, we see that the morphology of the two waveforms is rather different, see e.g., the slope of the signals near the peaks and valleys. One may understand these changes by looking at Equations (8) and (9) in [63]. There we see that the inclination angle enters in two different pieces. The first one, proportional to $1 + \cos^2 i$, is also present in quasi-circular mergers. However, the second piece, proportional to $\sim \sin^2 i$, is the one driving the changes in the morphology of the waveforms.

In Section IV we explore in detail the impact of the binary inclination angle in the SNR distributions of eccentric BBH mergers for second and third generation GW detector networks. We introduce a minimal set of data analysis tools we require for such analyses in the following section.

III. DATA ANALYSIS TOOLKIT

The SNR of a detector network is given by the sum of the power of the individual detectors [89]

$$\rho_N^2 = \sum_{k=1}^{N_D} \rho_k^2\,, \qquad (4)$$

where N_D is the number of detectors and where we define the individual SNRs as

$$\rho_k^2 = 2\int_{f_0}^{f_1} \frac{|h_k(f)|^2}{S_h(f)}\mathrm{d}f, \qquad (5)$$

where $h_k(f)$ is the waveform projected onto the k-th detector. Averaging over the polarization angle, ψ, we obtain

$$\langle\rho_N^2\rangle = 2\sum_k (F_{+,k}^2 + F_{\times,k}^2)\int_{f_0}^{f_1} \frac{|h(f)|^2}{S_h(f)}\mathrm{d}f, \qquad (6)$$

where $F_{+,k}$ and $F_{\times,k}$ are the antenna patterns of the individual detectors. As noted in [90], this integral does not depend on k and may therefore be taken outside the sum. Following the conventions described in [90], the antenna pattern functions are given by

$$F_+ = \sin\eta[a\cos(2\psi) + b\sin(2\psi)], \qquad (7)$$

$$F_\times = \sin\eta[b\cos(2\psi) - a\sin(2\psi)], \qquad (8)$$

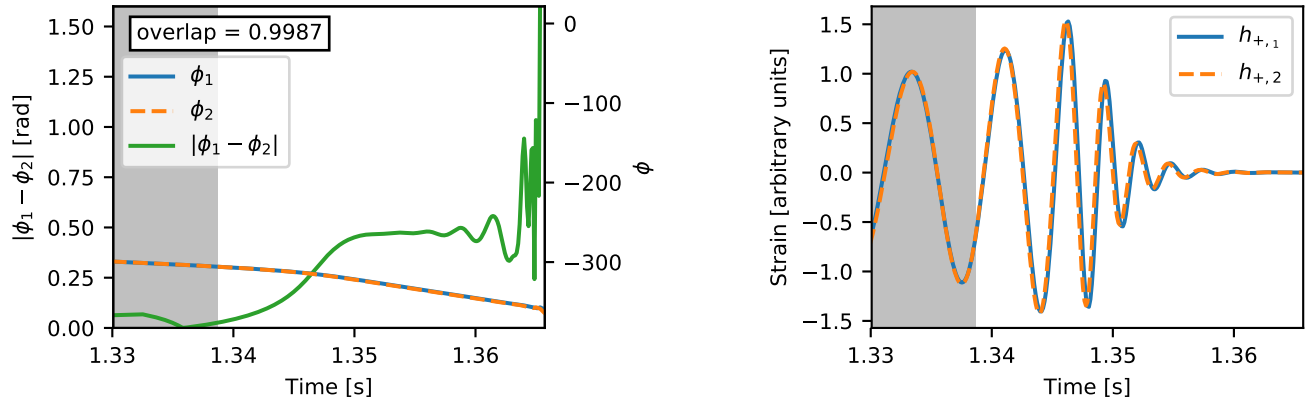where the functions a and b are given by

FIG. 1. Comparison between the original `ENIGMA` model in [62], and the model introduced in this article that has been recalibrated with the updated `SEOBNRv4` model found in LIGO's Algorithm Library [88]. The binary black hole system used for this comparison has total mass $M = 40\,M_\odot$, mass ratio $q = 4$, and initial eccentricity $e_0 = 0.1$ at a gravitational wave frequency $f_{\mathrm{GW}} = 25\,\mathrm{Hz}$. The left panel shows the phase difference $\phi_1 - \phi_2$ between the gravitational wave templates around the point in time where the merger-ringdown part is attached to the inspiral part. Differences before that point are due to using a different time integration method and interpolation scheme. Phase differences beyond that are due to the updated matching parameters obtained when recalibrating against `SEOBNRv4`. The right panel shows the + polarization of the gravitational wave strain during the same time interval. The shaded area is the pre-attachment inspiral region and the non-shaded area is the merger-ringdown part.
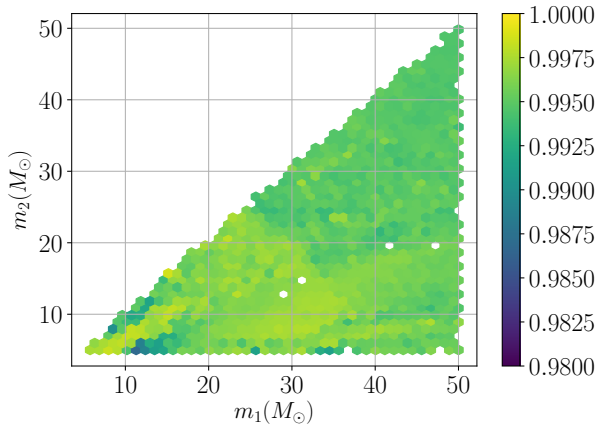
FIG. 2. Overlap distribution between `ENIGMA` and `SEOBNRv4_ROM` waveforms for component masses $5\,M_\odot \leq m_{\{1,2\}} \leq 50\,M_\odot$. These results were produced assuming advanced LIGO zero detuned high power PSD configuration, and setting a minimum gravitational wave frequency of $f_{\mathrm{GW}} = 15\,\mathrm{Hz}$ in Equation (2).
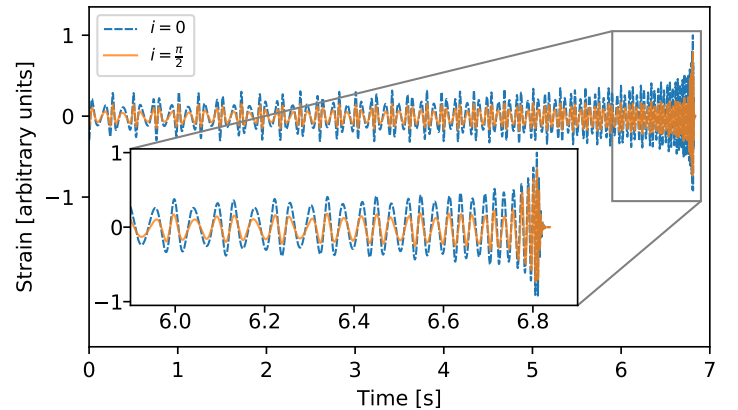

FIG. 3. Real part of the waveform strain produced by a binary black hole merger with parameters $e_0 = 0.3$ at a gravitational wave frequency of $f_{\mathrm{GW}} = 9\mathrm{Hz}$, mass-ratio $q = 3$ and total mass $M = 60\mathrm{M}_\odot$. Note the impact of the inclination angle in the amplitude of the waveform signal for two sample cases $i = \{0, \pi/2\}$.

Detector	Label	Longitude	Latitude	Orientation
LIGO Livingston	L	90° 46' 27.3" W	30° 33' 46.4" N	208.0° (WSW)
LIGO Hanford	H	119° 24' 27.6" W	46° 27' 18.5" N	279.0° (NW)
VIRGO, Italy	V	10° 30' 16" E	43° 37' 53" N	333.5° (NNW)
KAGRA, Japan	K	137° 10' 48" E	36° 15' 00" N	20.0° (WNW)
LIGO India	LI	74° 02' 59" E	19° 05' 47" N	270.0° (W)
AIGO, Australia	A	115° 42' 51" E	31° 21' 29" S	45.0° (NE)

TABLE I. Geographical location of the gravitational wave interferometers considered in this study.

$$a = \frac{1}{16}\sin(2\chi)[3 - \cos(2\beta)][3 - \cos(2\theta)]\cos[2(\phi + \lambda)]+$$
$$\frac{1}{4}\cos(2\chi)\sin(\beta)[3 - \cos(2\theta)]\sin[2(\phi + \lambda)]+$$
$$\frac{1}{4}\sin(2\chi)\sin(2\beta)\sin(2\theta)\cos(\phi + \lambda)+$$
$$\frac{1}{2}\cos(2\chi)\cos(\beta)\sin(2\theta)\sin(\phi + \lambda)+$$
$$\frac{3}{4}\sin(2\chi)\cos^2(\beta)\sin^2(\theta)\,, \tag{9}$$

$$b = \cos(2\chi)\sin(\beta)\cos(\theta)\cos[2(\phi + \lambda)]-$$
$$\frac{1}{4}\sin(2\chi)[3 - \cos(2\beta)]\cos(\theta)\sin[2(\phi + \lambda)]+$$
$$\cos(2\chi)\cos(\beta)\sin(\theta)\cos(\phi + \lambda)-$$
$$\frac{1}{2}\sin(2\chi)\sin(2\beta)\sin(\theta)\sin(\phi + \lambda)\,. \tag{10}$$

The source location is determined by the spherical coordinates on the sky, $(\theta,\,\phi)$; and $(\beta,\,\lambda)$ indicate the latitude and longitude location of GW detectors; the bisector of the GW detector's arms points in the χ direction which is measured counter-clockwise from East. The GW detector arms have an opening angle η. As described in [90], in this coordinate system the celestial coordinates $(\theta,\,\phi)$ are aligned with latitude and longitude in such a way that the equators of both systems coincide, and $(\theta = \pi/2,\,\phi = 0)$ is in the zenith direction above $(\beta = 0,\,\lambda = 0)$. In what follows, we present results for

$$\tilde{\rho} = \langle \rho_N^2 \rangle^{1/2}\,. \tag{11}$$

Furthermore, since we want to compare the SNR distribution of eccentric BBH populations with respect to quasi-circular BBH mergers, we will present our results using the metric

$$\Delta\tilde{\rho} = 100 \times \frac{\tilde{\rho}(e_0; \theta,\,\phi) - \tilde{\rho}(e_0 = 0; \theta,\,\phi)}{\tilde{\rho}_{\mathrm{LHV}}(e_0 = 0; \theta^*,\,\phi^*)}\,, \tag{12}$$

where $\tilde{\rho}(e_0; \theta,\,\phi)$ is the detector network SNR of a BBH system with initial eccentricity e_0 at a GW frequency f_0; $\tilde{\rho}(e_0 = 0; \theta,\,\phi)$ is the detector network SNR for the same BBH system but now assuming it is quasi-circular; and $\tilde{\rho}_{\mathrm{LHV}}(e_0 = 0; \theta^*,\,\phi^*)$ is the maximum SNR of a quasi-circular BBH population across the sky assuming a network consisting of GW detectors located at the LIGO Livingston (L), LIGO Hanford (H) and Virgo (V) sites— or LHV from now on.

IV. SIGNAL-TO-NOISE RATIO DISTRIBUTIONS FOR SECOND AND THIRD GENERATION GRAVITATIONAL WAVE DETECTOR NETWORKS

We consider second and third generation, ground-based GW detector networks, whose geographical locations are listed in Table I. We use the following nomenclature in Table I: LIGO Livingstone: L; LIGO Hanford: H; Virgo: V; KAGRA: K; LIGO India: LI; and a gravitational wave detector in Australia, AIGO, is labelled as A.

The PSD of each detector used in these studies was obtained from the open source files at [87, 91], and are shown in Figure 4. Note that we have assumed that the opening angle of all detectors is $\eta = \pi/2$. The actual networks we consider for second-generation GW detectors are:

- L+H+V. Herein we assume the target PSD for advanced LIGO for both L&H, and the target PSD for V.

- L+H+V+K. As the network above, and now also using the target PSD for K.
- L+H+V+K+LI+A. As the network above, and setting the PSDs for LI&A to be the same as for L.

For third generation detector networks that involve Cosmic Explorer [92] or the Einstein Telescope, we will consider the same geographical locations for individual detectors as listed in Table I, and replace PSD with the target sensitivity of Cosmic Explorer and the Einstein
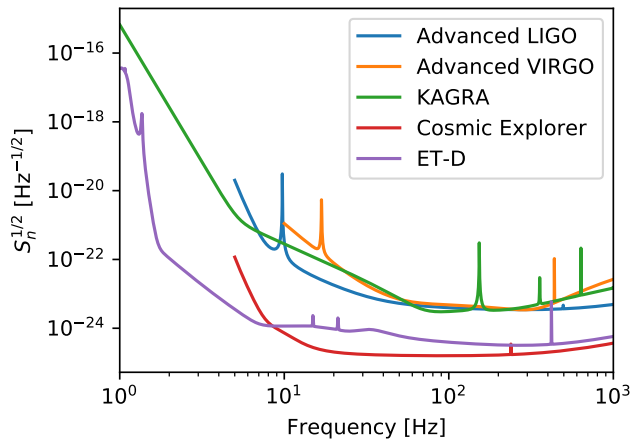
FIG. 4. Power Spectral Density configurations of advanced LIGO, advance Virgo, Kagra, Cosmic Explorer, and the Einstein Telescope. We used the data provided in [87, 91] to model the sensitivity of these second and third generation gravitational wave detectors.

Telescope, configuration D (ET-D) [93, 94], as described in [87, 91].

To motivate the results we present in the following sections, in Figure 5 we present a waveform that describes the merger of a BBH with component masses $(50M_\odot, 10M_\odot)$, and $e_0 = 0.5$ at $f_{GW} = 4$ Hz. The signal is whitened with the target PSDs for advanced LIGO, Cosmic Explorer and the ET-D. We notice that Cosmic Explorer and ET-D magnify amplifications in the amplitude of the waveform that are driven by orbital eccentricity. The key point is that these amplifications occur at lower frequencies, or early times in the waveform signal, in such a way that when we compute the SNR of these eccentric mergers, amplitude magnifications compensate for the shrinkage in timespan that is also driven by orbital eccentricity. For this particular case, *this eccentric waveform is just a fifth the length of its quasi-circular counterpart.* However, as we discuss below, the SNR of eccentric and quasi-circular systems are comparable. These observations will drive the presentation of our results in the following sections.

A. SNR distributions for second generation detector networks

In this section we present our findings for second generation detector networks. We have found that we can extract the most physics from the observation of eccentric BBH mergers when we take into the account two key properties that drive the evolution of eccentric mergers, i.e., the reduction in the length of waveform signals, and the rate at which SNR is accumulated.

To motivate this discussion, Figure 6 presents SNR distributions of eccentric BBH mergers, normalized with

respect to quasi-circular BBH systems, assuming eccentricities $e_0 \leq 0.5$ measured at $f_{GW} = 9$Hz. The SNR distributions are computed by setting $f_0 = 11$ Hz and $f_1 = 4096$ Hz in Eq. (5), and assuming a single advanced LIGO detector.

The panels in Figure 6 present results for BBH systems with total masses $20M_\odot \leq M \leq 100M_\odot$ and mass-ratios $1 \leq q \leq 5$. These panels show the interplay between total mass and mass-ratio in the SNR distribution of eccentric mergers. These results show that heavier binaries have larger SNRs, and that they tend to have shorter duration in band. These results show that the SNR of eccentric mergers will be between $[0.8-1.2] \times$SNR of quasi-circular mergers that have the same mass-ratio and total mass. The most dramatic finding in these studies is that for these extreme scenarios in which the SNR of $e_0 \sim 0.5$ mergers is similar to quasi-circular events, the waveform length of eccentric systems is about eight times shorter for equal mass systems, and five times shorter for $q = 5$ systems. In other words, the rate at which SNR is accumulated for eccentric mergers is significantly faster than for quasi-circular mergers. We will study this point in further detail below.

In order to provide a visual representation of the importance of having access to a global detector network, we have quantified the SNR sky distribution for a few sample cases with component masses $m_{\{1, 2\}} = \{(30M_\odot, 30M_\odot), (50M_\odot, 10M_\odot)\}$, with eccentricities $e_0 \leq 0.5$ measured at $f_{GW} = 9$Hz. The SNR distributions are computed by setting $f_0 = 11$ Hz and $f_1 = 4096$ Hz in Eq. (5). Highlights of these results include:

- Figure 7 shows that for systems with component masses $(30M_\odot, 30M_\odot)$, a gradual increase in eccentricity drives a corresponding boost in SNR. This effect reaches a maximum for $e_0 = 0.4$, with a net SNR increase of ΔSNR $\sim 12\%$ with respect to quasi-circular systems. Systems with larger eccentricity, $e_0 = 0.5$, have similar SNRs than quasi-circular mergers. In other words, for $e_0 \geq 0.4$ BBH mergers the increase in amplitude of the signal at lower frequencies no longer compensates for the shrinkage in the waveform length. We can extract this information by looking at the sky maps from top to bottom. If we now look at them from left to right, we learn that a larger detector network increases the loudness of signals across the sky, while also forming distinct detection hot spots, e.g., see the sky map for $e_0 = 0.4$ assuming a 6 detector network.

- Figure 8 shows that asymmetric mass-ratio BBH mergers produce louder mergers than comparable mass-ratio systems for larger values of eccentricity. In this case, $(50M_\odot, 10M_\odot)$ systems report a net increase in SNR, ΔSNR $\sim 30\%$ for $e_0 = 0.5$.
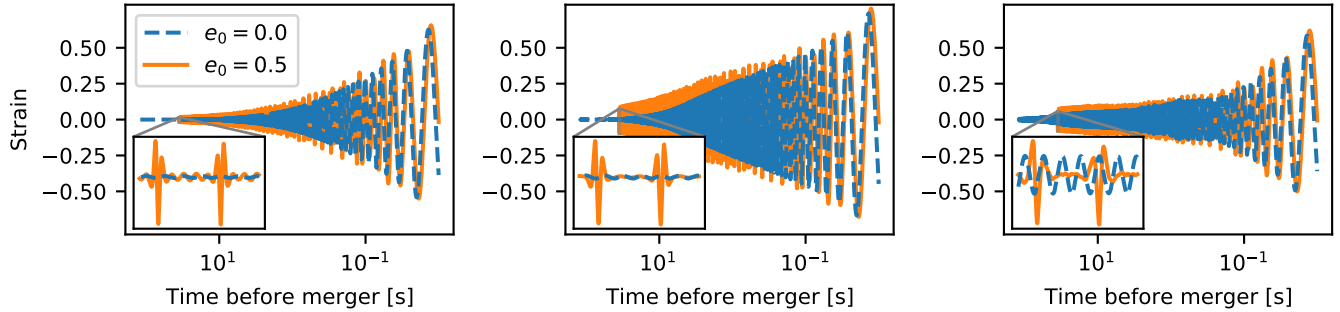
FIG. 5. Effect of the power spectral sensitivity of Advanced LIGO (left), Cosmic Explorer (center) and ET-D (right) on a waveform signal that describes a binary system with component masses $(50M_\odot, 10M_\odot)$, and eccentricity of $e_0 = 0$ (blue, dashed curve) and $e_0 = 0.5$ (orange, solid curve), both measured at a gravitational wave frequency $f_{GW} = 4\,Hz$. The quasi-circular signal is 126.27s long, while the eccentric signal is 37.32s long. Eccentricity-driven amplitude amplifications are clearly noticeable throughout the entire evolution (the orange signal is louder throughout, see also insets which show data in a 1s interval at the beginning of the eccentric signal). Data are normalized to have a maximum amplitude of unity.
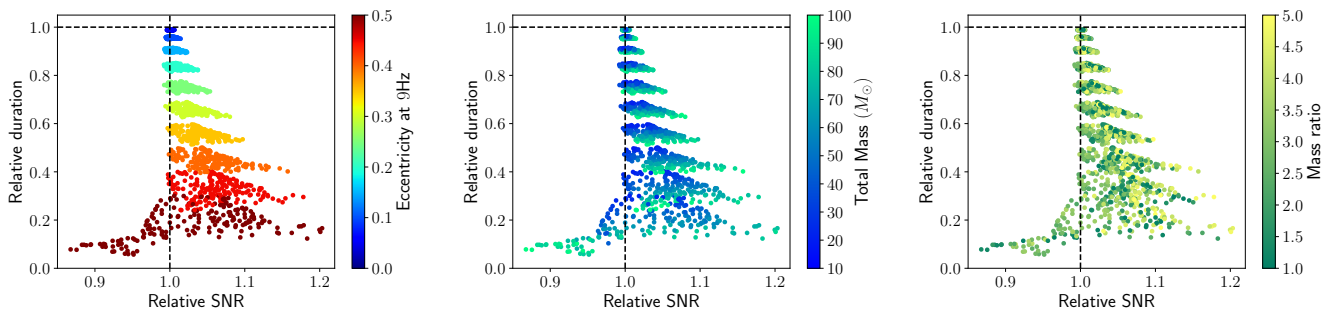
FIG. 6. Length and signal-to-noise-ratio of eccentric binary black hole mergers relative to quasi-circular systems. Both panels show systems with total mass $20M_\odot \leq M \leq 100M_\odot$ and mass-ratios $1 \leq q \leq 5$. In these panels, `Relative SNR` $\to$ `SNR(eccentric)/SNR(quasi-circular)`, and `Relative duration` $\to$ `duration(eccentric)/duration(quasi-circular)`.
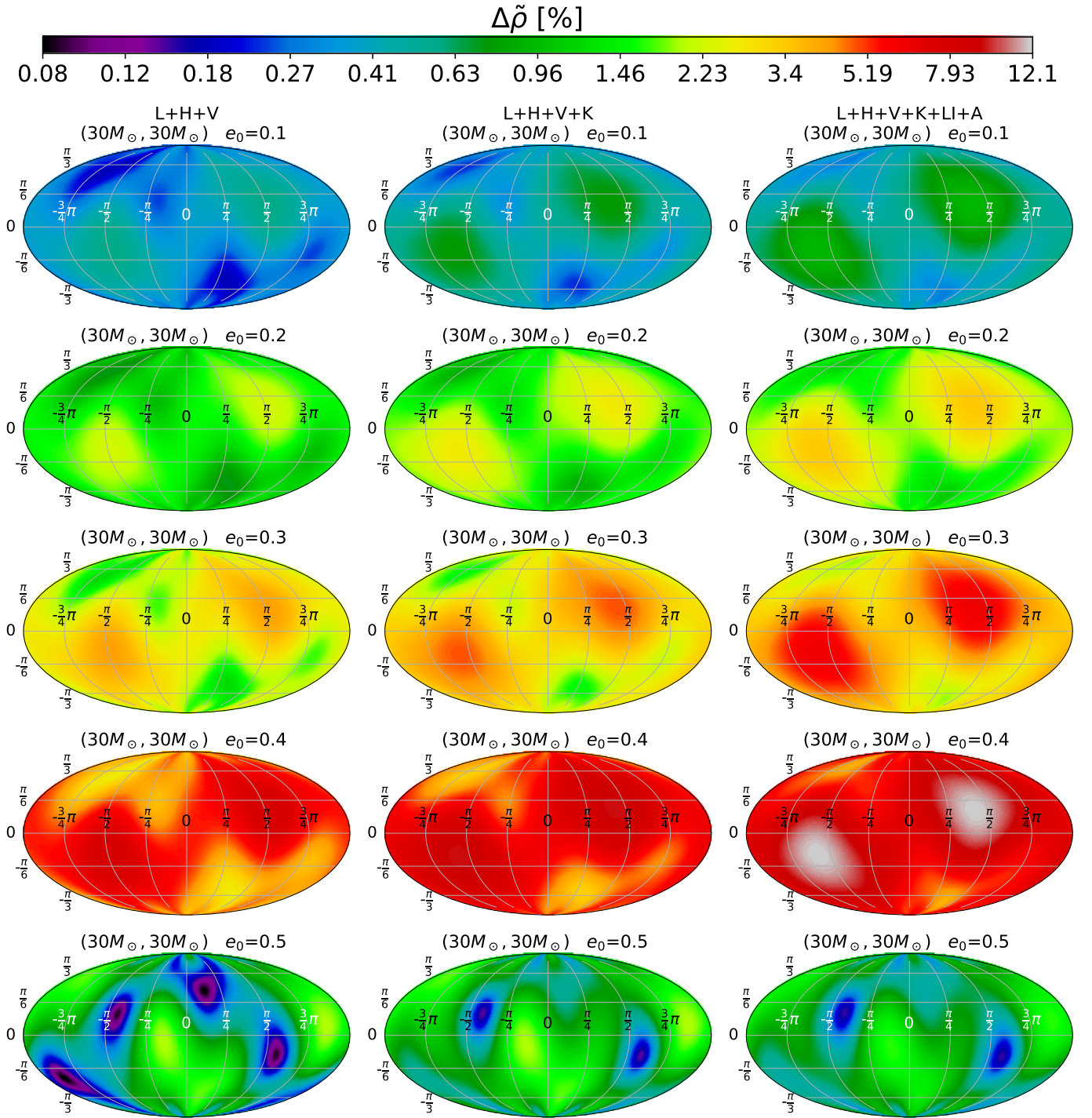
FIG. 7. Using the metric provided in Eq. 12, these sky maps show the relative signal-to-noise difference between eccentric and quasi-circular black hole mergers with component masses $(30\mathrm{M}_\odot, 30\mathrm{M}_\odot)$. We use the Mollweide projection $(\vartheta, \varphi) \rightarrow (\pi/2 - \theta, \phi - \pi)$, averaged over polarization angles, and set the binary inclination angle to $i = \pi/4$. The range of eccentricity increases from top to bottom, while the size of the detector network increases from left to right. Additional results for $i = 0$ are presented in Appendix A.
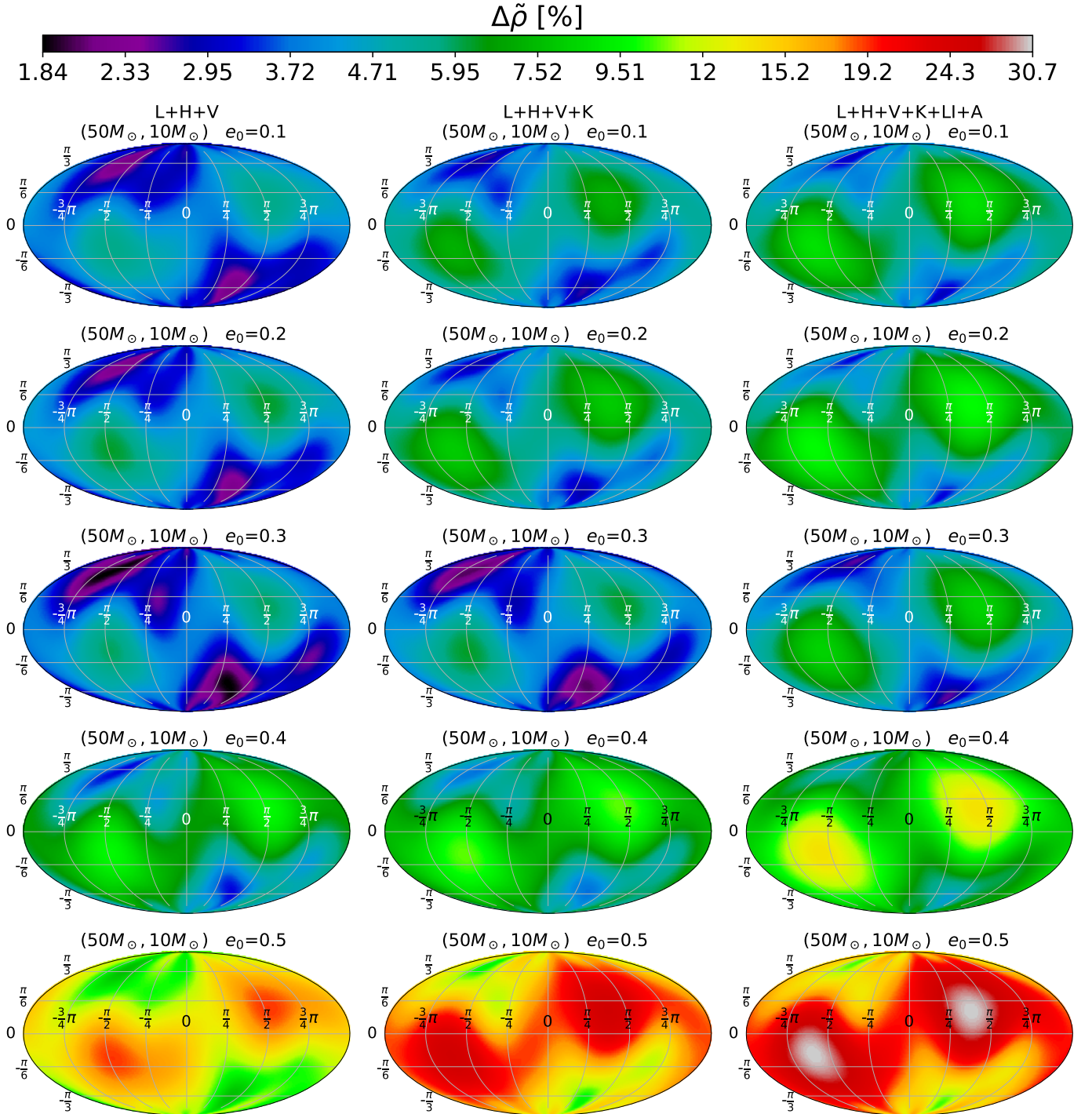
FIG. 8. As Figure 7 but now for black hole mergers with component masses $(50\mathrm{M}_\odot, 10\mathrm{M}_\odot)$.

B. Third generation detector networks

We consider two configurations for third generation detector networks. In these two cases the geographical location of the GW detectors is identical to those listed in Table I. The only difference is that we replace the PSD of each of these detectors using the target sensitivity of either Cosmic Explorer or ET-D.

Cosmic Explorer This is a proposed L-shaped detector, based in the US, whose arms will be 10 times longer that advanced LIGO's. Details regarding Cosmic Explorer's layout, scale, technology and science scope may be found at [95].

To provide a high level description of the importance of eccentricity, total mass and mass-ratio for the observation of BBH mergers, we consider a single Cosmic Explorer detector, and compute the SNR and waveform length of BBH systems with total mass $20\mathrm{M_\odot} \leq M \leq 100$, mass-ratios $1 \leq q \leq 5$, and $e_0 \leq 0.5$ measured at $f_{\mathrm{GW}} = 9\,\mathrm{Hz}$. We compute SNR distributions setting $f_0 = 11\,\mathrm{Hz}$ and $f_1 = 4096\,\mathrm{Hz}$ in Eq. (5). We have set these parameters for the computation of SNR to provide a direct comparison to advanced LIGO-type detectors. The key difference is that Cosmic Explore provides enhanced sensitivity at lower frequencies, as shown in Figure 4. These results, presented in the top panels of Figure 9, show that the SNR distributions of eccentric and quasi-circular mergers are comparable up to eccentricities $e_0 \leq 0.4$. However, there is a significant drop in SNR for systems with $e_0 \sim 0.5$.

We also provide results to visualize the SNR sky distribution for a detector network of Cosmic Explorers for two cases that describe BBH mergers with component masses $m_{\{1, 2\}} = \{(30\mathrm{M_\odot}, 30\mathrm{M_\odot}), (50\mathrm{M_\odot}, 10\mathrm{M_\odot})\}$, with eccentricities $e_0 \leq 0.5$ measured at $f_{\mathrm{GW}} = 9\mathrm{Hz}$. The SNR distributions are computed by setting $f_0 = 11\,\mathrm{Hz}$ and $f_1 = 4096\,\mathrm{Hz}$ in Eq. (5). Relevant findings include:

- Figure 10 shows that, for equal mass-ratio BBH mergers, eccentric and quasi-circular systems have comparable SNR sky distributions for $e_0 \leq 0.4$. We notice that in some cold spots, quasi-circular systems are $\sim 34\%$ louder than $e_0 = 0.5$ BBH systems. Compared to similar systems presented in Figure 7 for second generation detector networks, we notice that Cosmic Explorer will be able to clearly tell apart these two types of populations through their SNR distributions for eccentricities $e_0 \geq 0.4$.

- Figure 11 presents SNR sky distributions for BBH mergers with masses $(50\mathrm{M_\odot}, 10\mathrm{M_\odot})$. These results show that larger mass-ratios tend to attenuate SNR suppression for the most eccentric systems. Notice that while for equal mass-ratio systems with $e_0 \sim 0.5$ the SNR drops by $\sim 36\%$, in this case the SNR is $\sim 24\%$ the SNR of quasi-circular mergers with identical total mass and mass-ratio. This finding is also consistent with results presented for second generation detector networks.

In summary, we find that in the context of the Cosmic Explorer, the SNR of eccentric and quasi-circular BBH mergers is comparable for eccentricities $e_0 \geq 0.4$. As we discuss in the following section, we can disentangle this apparent similarity when we look at the rate at which SNR is accumulated. We also find that quasi-circular mergers are significantly louder than eccentric ones for $e_0 \sim 0.5$.

Einstein Telescope D This is a proposed third generation detector, based in Europe, that aims to improve the target sensitivity of advanced LIGO-type detectors by an order of magnitude. In this study, we assume a geometry in which the detectors arms are 10km long, L-shaped, and consider the ET-D sensitivity curve for all calculations. Information regarding the conceptual design and the fundamental physics that may be accomplished with the Einstein Telescope may be found at [96, 97].

As we did for Cosmic Explorer, we begin this discussion by providing a high level overview of the detectability of eccentric BBH mergers with ET-D. It is worth mentioning that given the planned sensitivity for ET-D at lower frequencies, we can now produce waveforms from $f_{\mathrm{GW}} = 4\,\mathrm{Hz}$, which enables us to explore systems with a broader range of eccentricities, e.g., $e_0 \leq 0.6$. We compute the SNR distributions setting $f_0 = 5\,\mathrm{Hz}$ and $f_1 = 4096\,\mathrm{Hz}$ in Eq. (5).

The bottom panels in Figure 9 show that the SNR of eccentric and quasi-circular systems is comparable for eccentricities $e_0 \leq 0.5$. This is worth highlighting in view that eccentric BBH mergers with $e_0 \sim 0.5$ had significantly lower SNRs than quasi-circular mergers with identical total mass and mass-ratio when observed with Cosmic Explorer. In the case of ET-D, we find that quasi-circular BBH mergers become louder than eccentric mergers for $e_0 \sim 0.6$. We may understand this result if we consider that the improved sensitivity of ET-D at lower frequencies amplifies the enhancement in the waveform signal, driven by eccentricity corrections, thereby compensating for the signal reduction of such highly eccentric systems.

We have also produce SNR sky distributions for ET-D detector networks. For consistency, we present results for systems with component masses $m_{\{1, 2\}} = \{(30\mathrm{M_\odot}, 30\mathrm{M_\odot}), (50\mathrm{M_\odot}, 10\mathrm{M_\odot})\}$, with eccentricities $e_0 \leq 0.6$ are measured at $f_{\mathrm{GW}} = 4\mathrm{Hz}$. The SNR distributions are computed by setting $f_0 = 5\,\mathrm{Hz}$ and $f_1 = 4096\,\mathrm{Hz}$ in Eq. (5). Some observations we draw from these results include:

- We notice that for equal mass binaries, Figure 12, the SNR sky distributions of quasi-circular and eccentric mergers are comparable for eccentricities in the range $e_0 < 0.5$. This is truly remarkable if one considers that these eccentric systems have less than half the timespan of their quasi-circular counterparts. These results underscore the impact that third generation GW detectors will have at boosting the amplitude amplifications driven by eccentricity at lower frequencies, which will actually
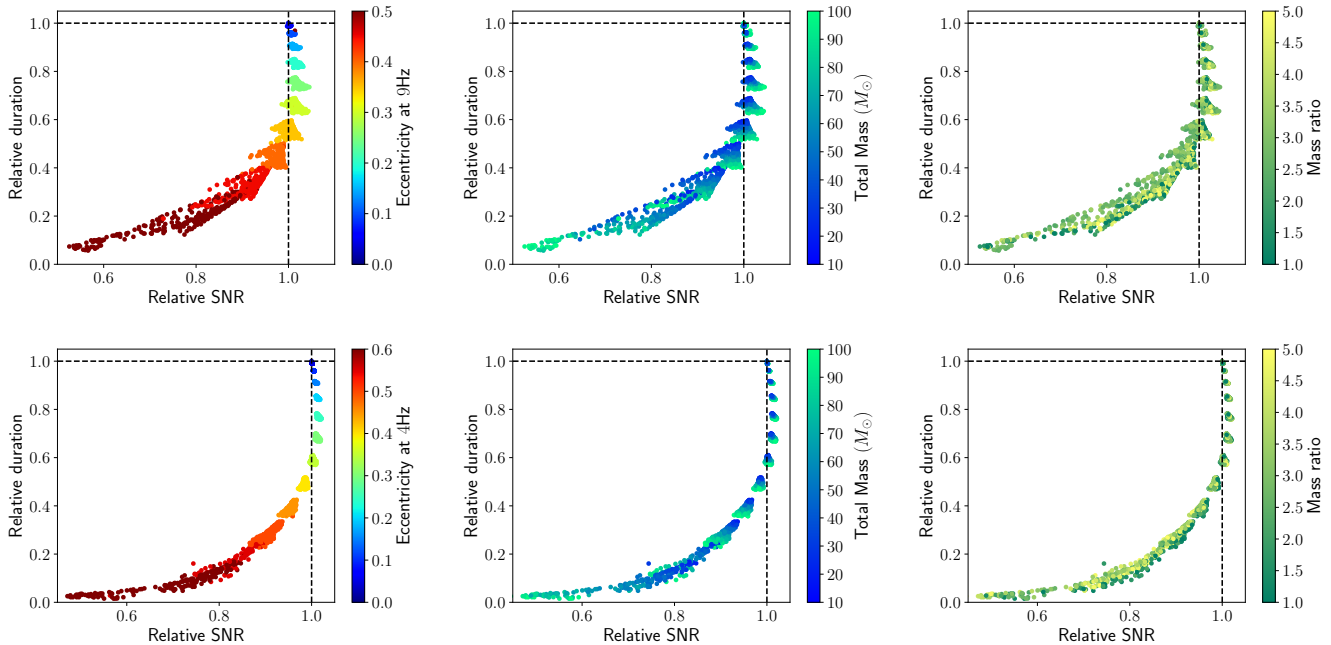
FIG. 9. As Figure 6, but now for Cosmic Explorer (top panels) and ET-D (bottom panels). As before, these results present systems with total mass $20\mathrm{M}_\odot \leq M \leq 100\mathrm{M}_\odot$ and mass-ratios $1 \leq q \leq 5$.

compensate for the dramatic reduction in waveform timespan for signals with $e_0 \sim 0.5$.

- As we have discussed before, asymmetric mass-ratio systems tend to attenuate the SNR suppression in eccentric mergers. For instance, for the most eccentric systems in our sample, see Figure 13, the SNR reduction for $e_0 \sim 0.6$ mergers is about 40% the SNR of an equivalent system with zero eccentricity. In contrast, Figure 12 shows that for comparable mass-ratio mergers, quasi-circular systems are 50% louder than $e_0 \sim 0.6$ BBH mergers with the same total mass and mass-ratio.

These results present a number of unique properties of eccentric mergers that may be used to differentiate them from quasi-circular BBHs. It is worth mentioning that while spin corrections may mimic the physics of moderately eccentric mergers, as shown in [63], the effects of eccentricity we have discussed are unique for moderate values of eccentricity for second or third generation GW detector networks. No spin effects are capable of amplifying the waveform amplitude and shortening the waveform timespan in the way shown in Figures 5, 6, and 9, or to accelerate the accumulation of SNR at the rate we presented in this section.

V. CONCLUSIONS

We have introduced an improved version of the `ENIGMA` model that provides a numerically stable approach to attach the merger waveform to the inspiral evolution, as well as the inclusion of the binary inclination angle, which is a key feature that not only modifies the amplitude evolution of eccentric mergers, but also encodes additional physics even at leading order post-Newtonian corrections. We have tested the robustness of our waveform generator, finding that we can randomly sample the $m_{\{1,2\}} \in [5\mathrm{M}_\odot, 50\mathrm{M}_\odot]$ parameter space, varying the inclination angle, and produce over 1M physically consistent waveforms without reporting any errors. We then established its accuracy in the quasi-circular limit by computing overlaps with the `SEOBNRv4` model, finding overlaps $\mathcal{O} \geq 0.99$ over the parameter space of applicability for `ENIGMA`. We benchmarked `ENIGMA`, finding that, averaged over 1000 iterations, it can produce a single waveform from $f_{\mathrm{GW}} = 15\,\mathrm{Hz}$ at a sample rate of $8192\,\mathrm{Hz}$ within 0.04 seconds.

We then explored the properties of SNR sky distributions produced by eccentric and quasi-circular BBH mergers in the context of second and third generation GW detectors. Our results indicate that SNR sky distributions tend to present eccentric and quasi-circular mergers as similar events, which may only be differentiated for rather eccentric BBH populations. We have introduced a complementary method to tell apart these two populations that consists of studying the rate at which SNR accumulates in eccentric mergers, demonstrating that such approach exhibits tell-tale signatures that may not be mimicked by other orbital effects, such as spin corrections.

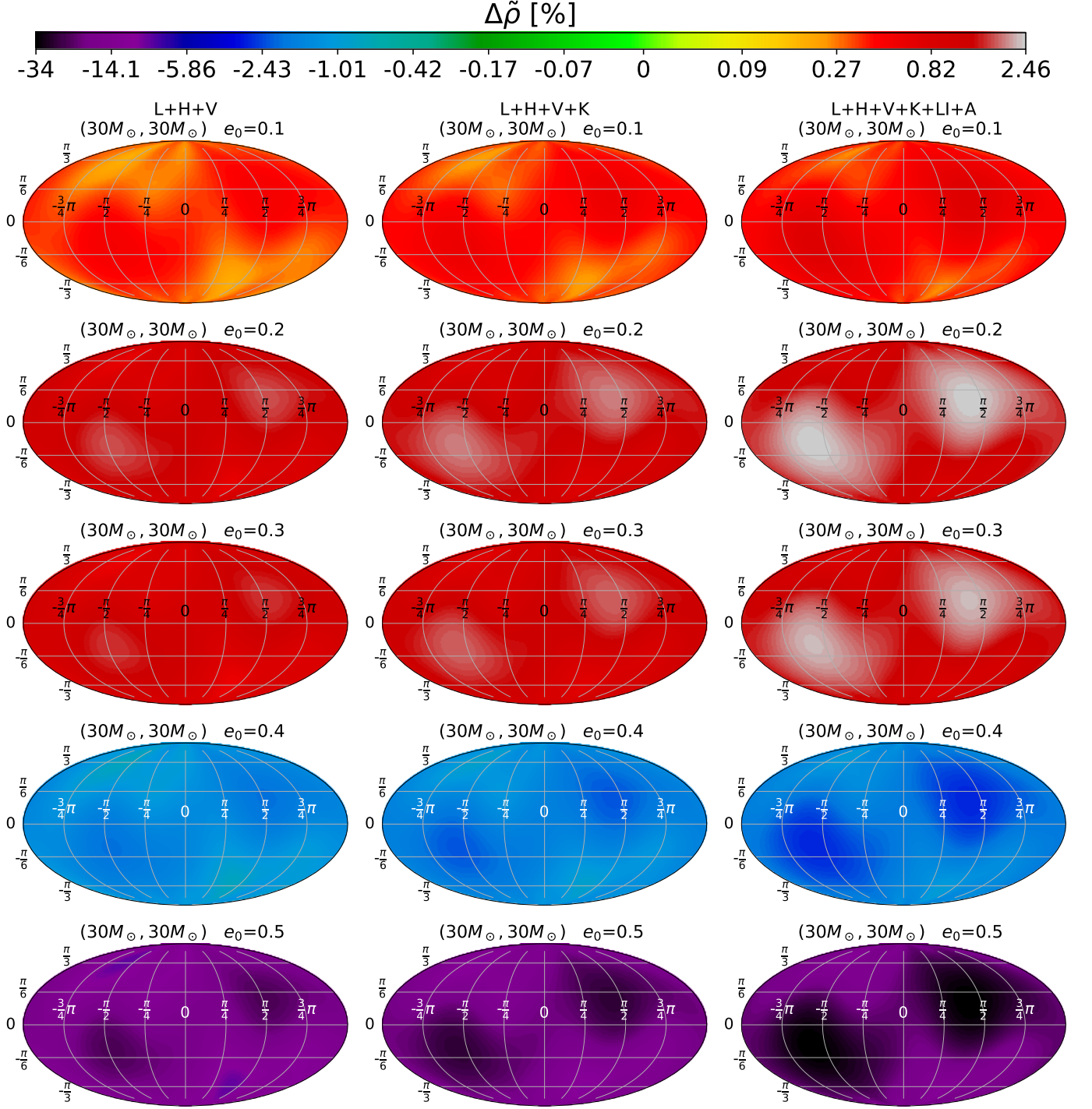With these studies we introduce a ready-to-use `ENIGMA`

FIG. 10. As Figure 7, but now assuming that the PSD of each detector corresponds to the target sensitivity of Cosmic Explorer. These results are produced assuming binary black hole mergers with component masses (30M$_\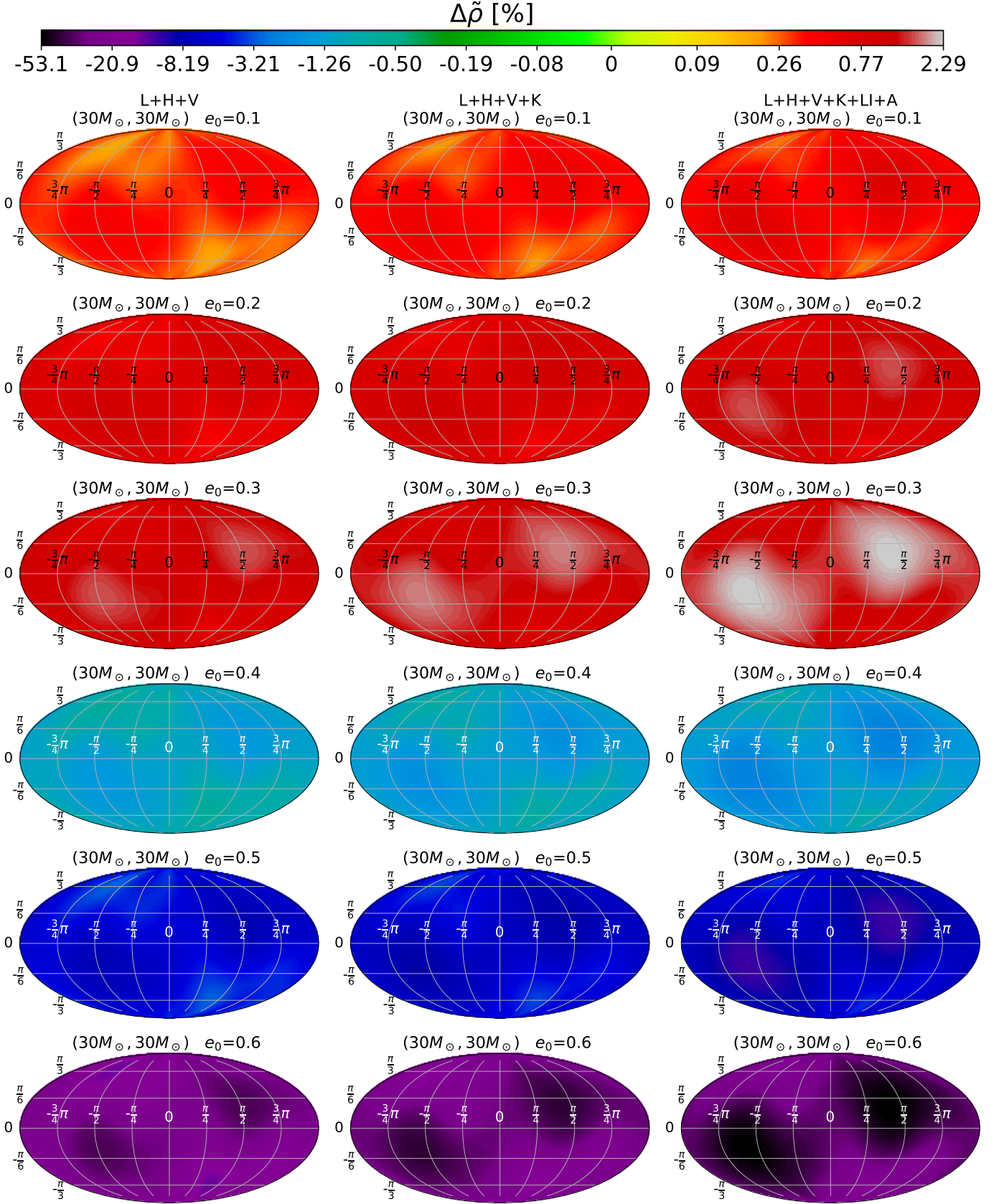odot$, 30M$_\odot$). As before, we have used the Mollweide projection, averaged over polarization angles, and set the binary inclination angle to $i = \pi/4$. See Appendix A for results assuming $i = 0$.

model that may be readily put at work to conduct GW searches of eccentric events in similar manner to those presented in [52, 98], or to constrain the eccentricity of all BBH mergers detected by LIGO and Virgo to date. It may be timely and relevant to assess the use of `ENIGMA` waveforms to recover the astrophysical parameters of eccentric BBH mergers using well characterized eccentric numerical relativity waveforms [69–71, 73] embedded in real advanced LIGO noise to quantify the biases that are introduced by noise and intrinsic waveform errors in parameter estimation studies. These studies will be pursued in the near future.

VI. ACKNOWLEDGMENTS

$\Delta\tilde{\rho}$ [%]

-22.1   -8.62   -3.36   -1.31   -0.51   -0.20   -0.08   0   0.08   0.20   0.53   1.39   3.61

FIG. 11. As Figure 10 but now for component masses $(50\mathrm{M}_\odot, 10\mathrm{M}_\odot)$.

$$\Delta\tilde{\rho}\ [\%]$$

| -53.1 | -20.9 | -8.19 | -3.21 | -1.26 | -0.50 | -0.19 | -0.08 | 0 | 0.09 | 0.26 | 0.77 | 2.29 |

FIG. 12. As Figure 7, but now assuming that the PSD of each detector corresponds to the target sensitivity of ET-D. These results are produced assuming binary black hole mergers with component masses $(30\mathrm{M}_\odot, 30\mathrm{M}_\odot)$. As before, we have used the Mollweide projection, averaged over polarization angles, and set the binary inclination angle to $i = \pi/4$. See Appendix A for results assuming $i = 0$.
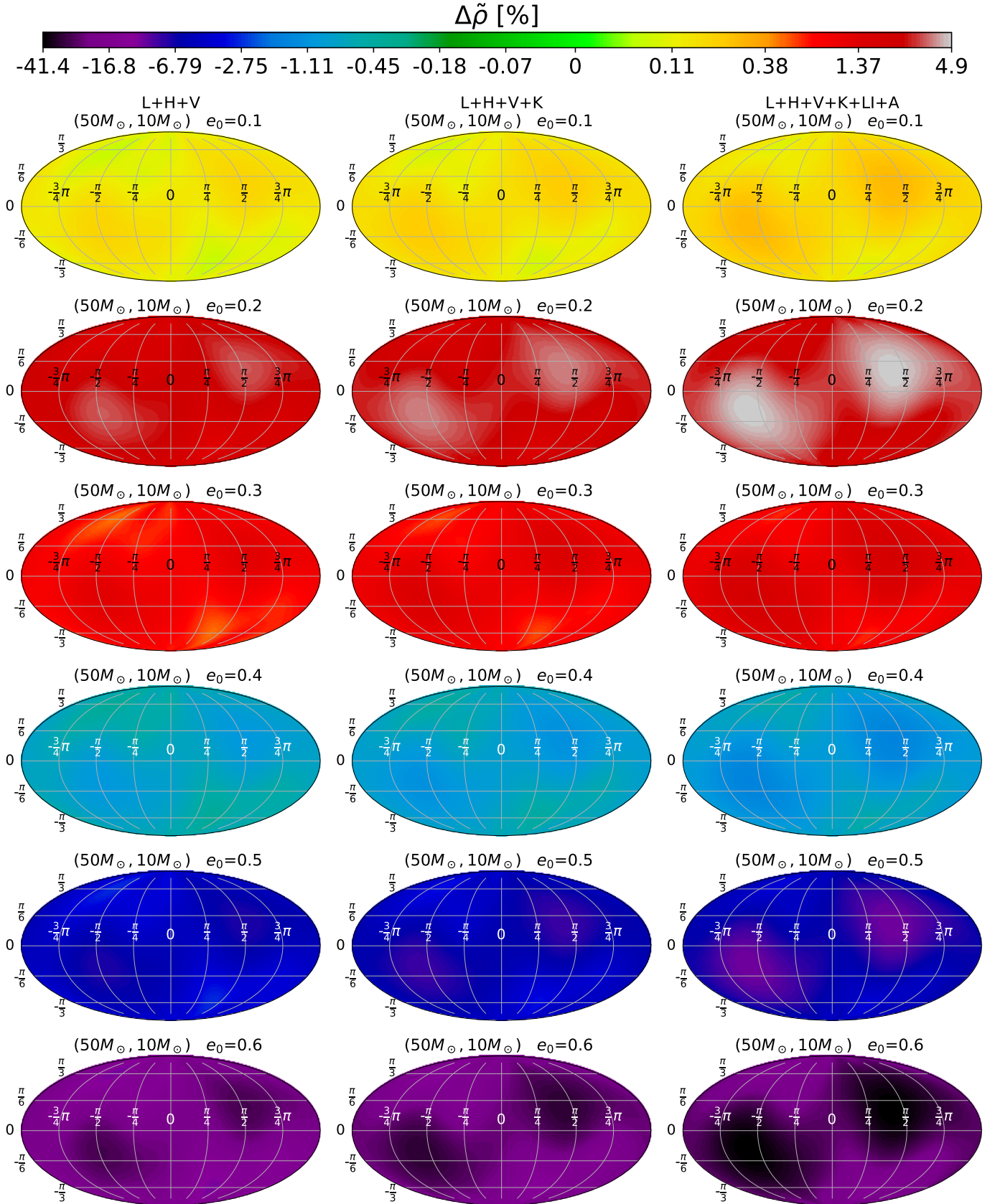
FIG. 13. As Figure 12 but now for component masses $(50 \mathrm{M}_\odot, 10 \mathrm{M}_\odot)$.
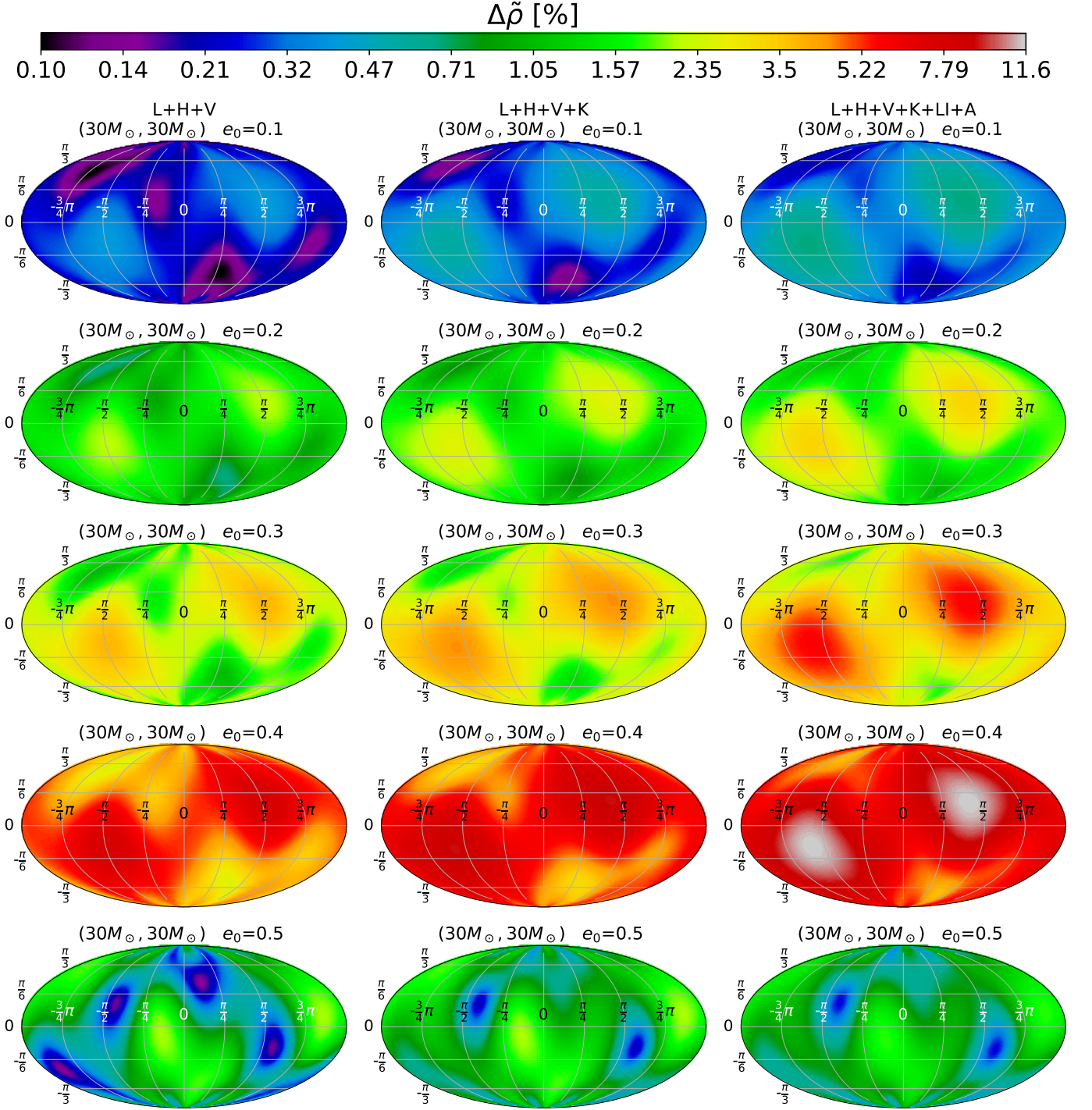
FIG. 14. As Figure 7 but now setting the binary inclination angle to 0.

Appendix A: Additional signal-to-noise sky distributions for eccentric binary black hole mergers

In this section we present SNR sky distributions for eccentric BBH mergers with inclination angle $i = 0$. These results mirror those we presented in the main body of the article for second and third generation GW detector networks.
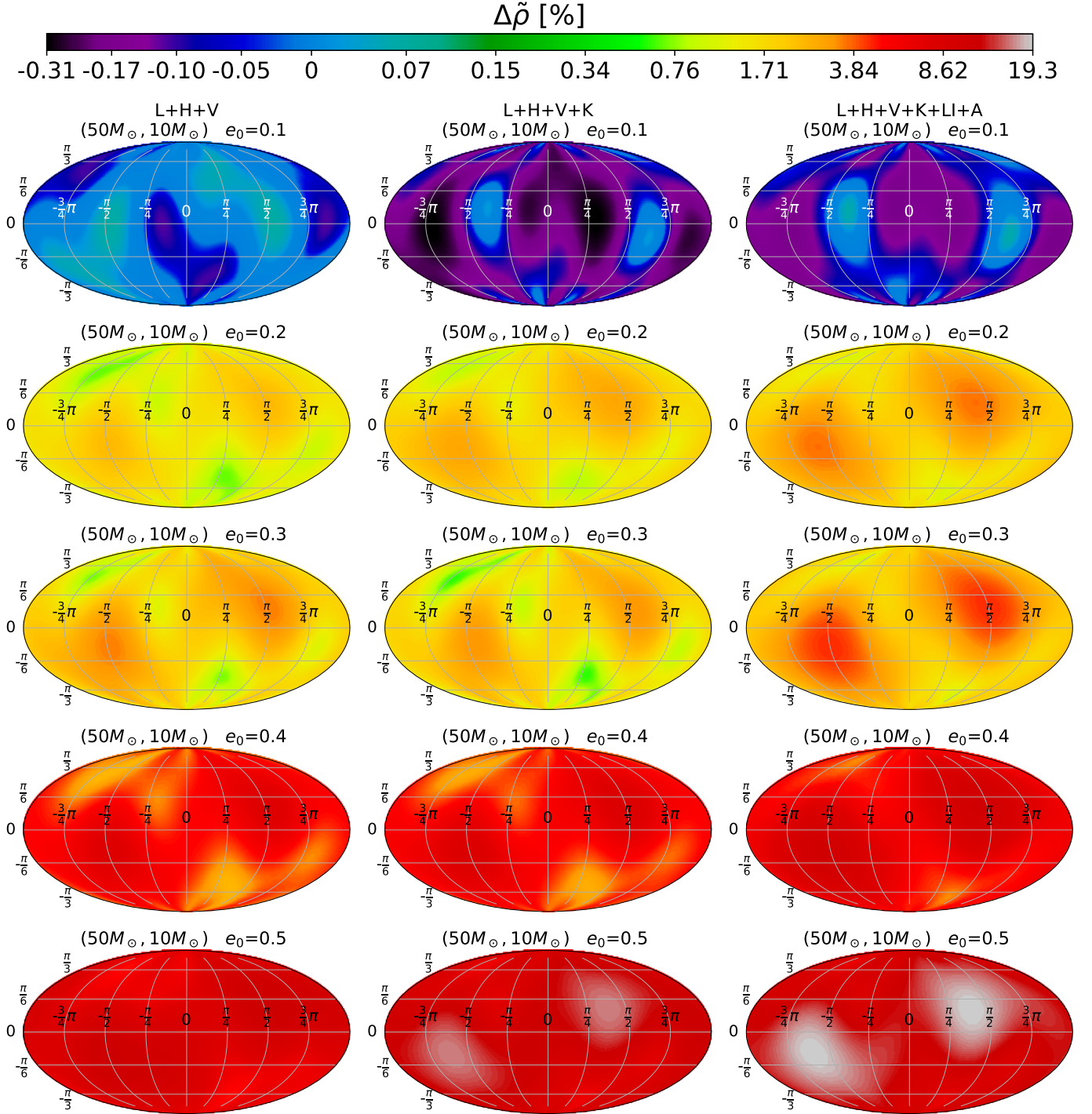
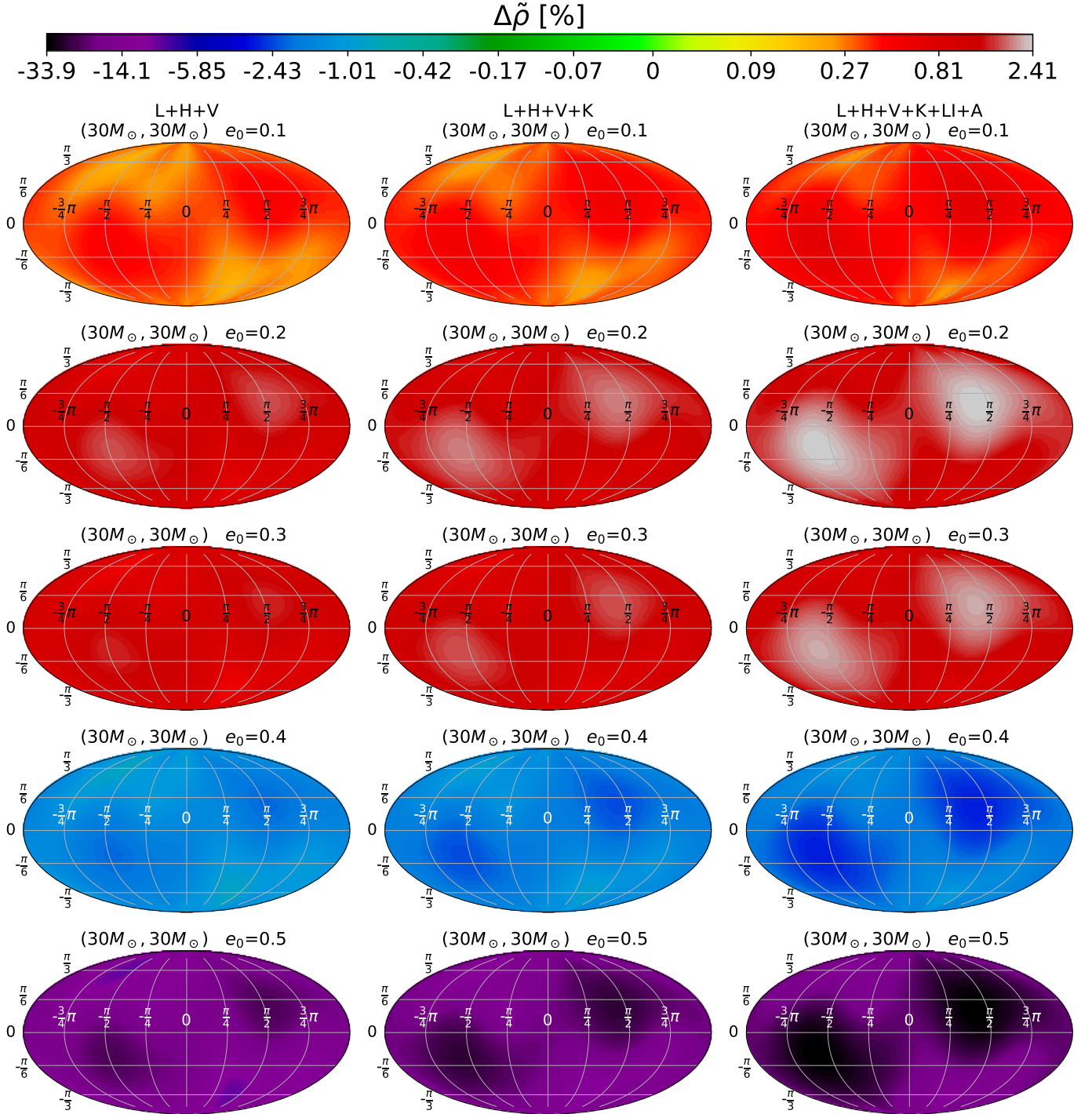FIG. 15. As Figure 14 but now for component masses $(50 M_\odot, 10 M_\odot)$.

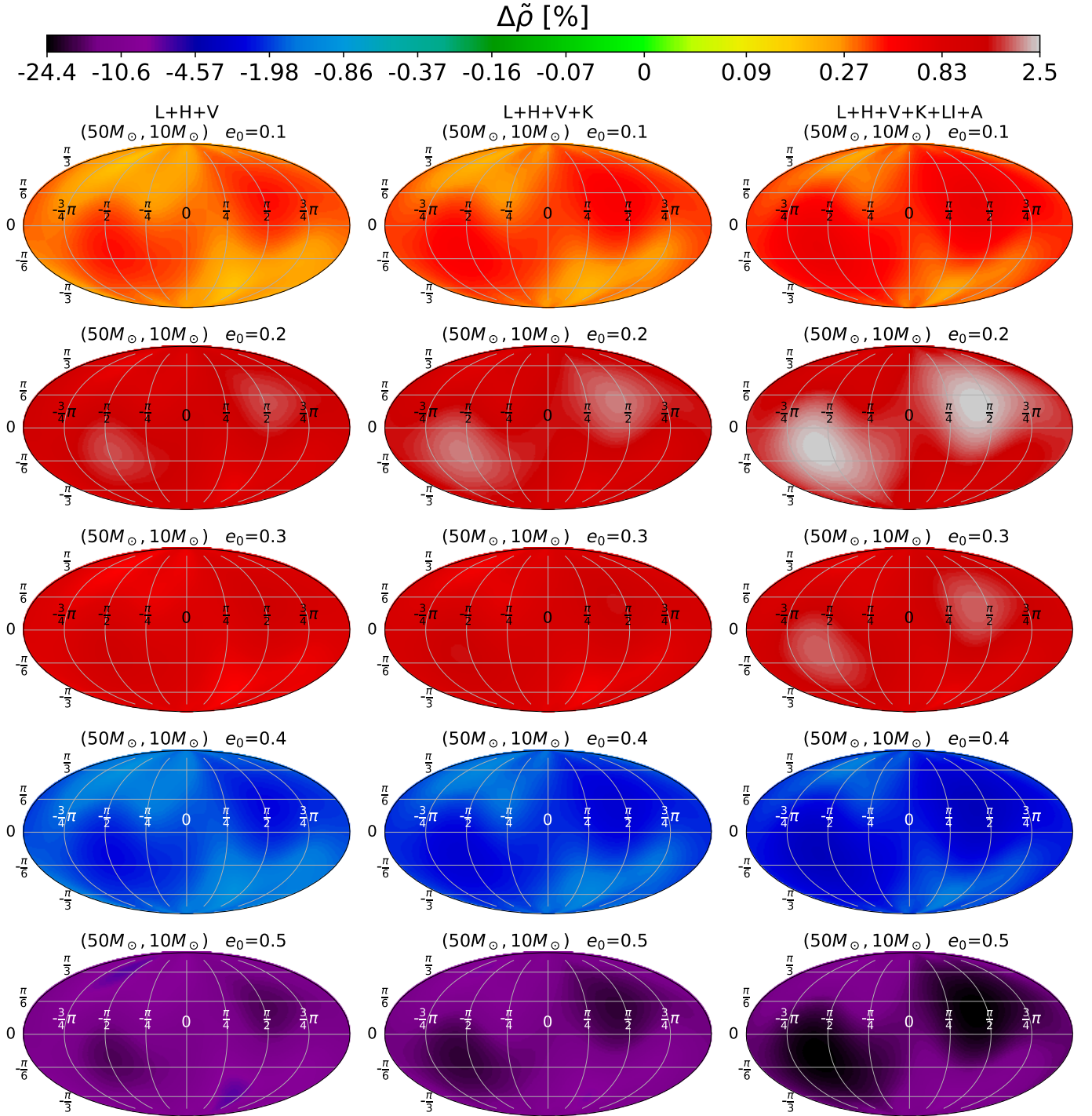FIG. 16. As Figure 10 but now setting the binary inclination angle to 0.

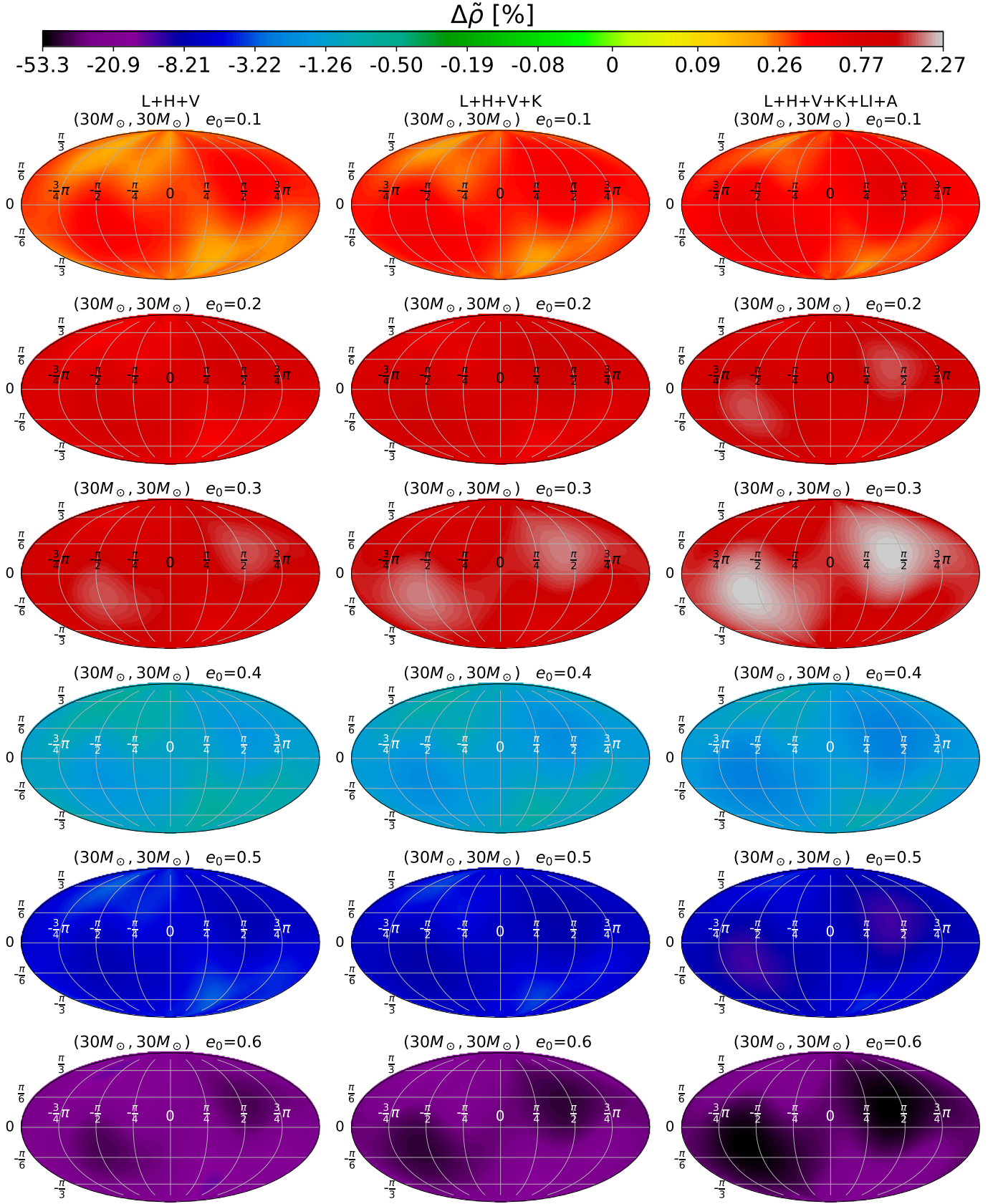FIG. 17. As Figure 16 but now for component masses (50M$_\odot$, 10M$_\odot$).

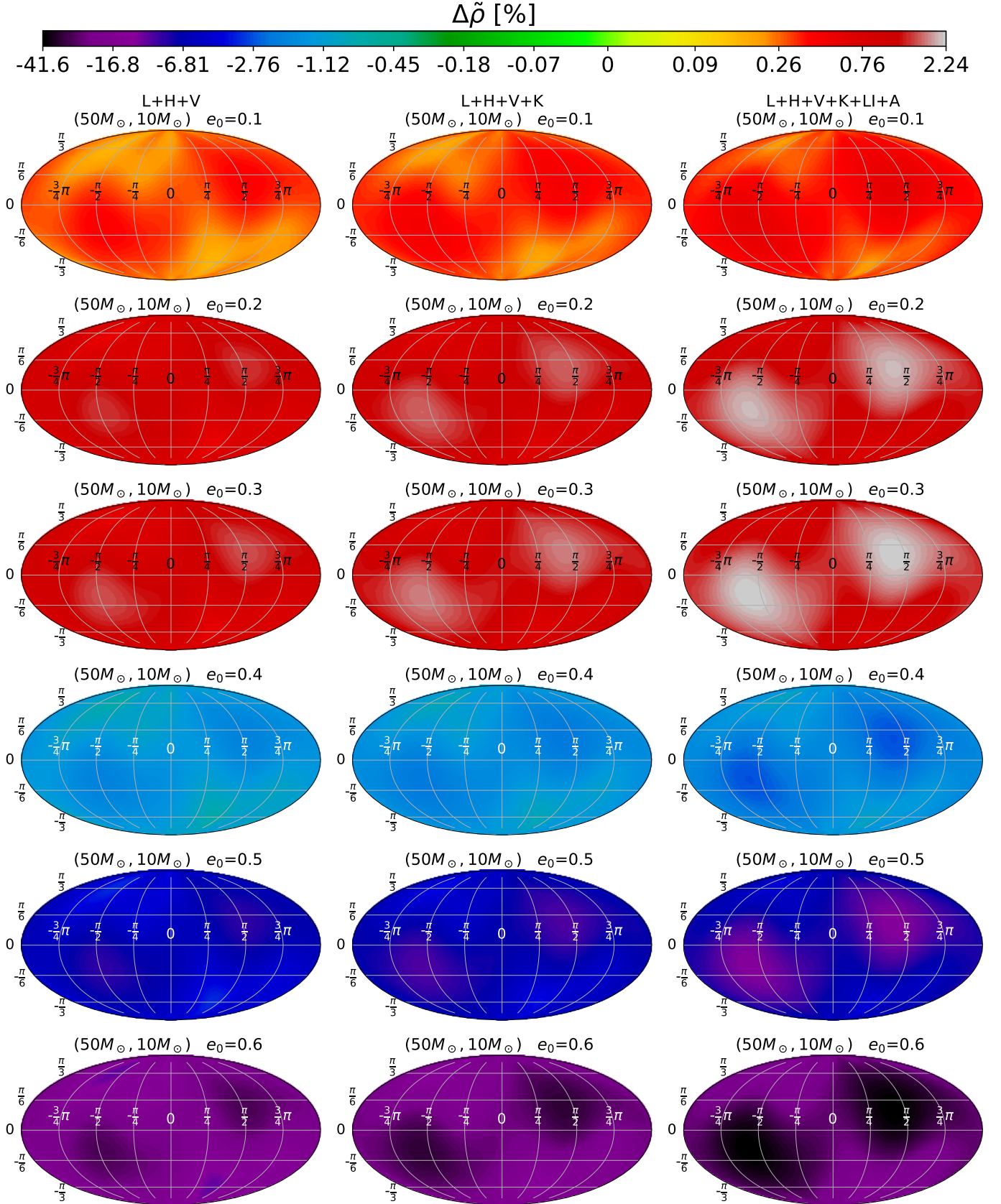FIG. 18. As Figure 12 but now setting the binary inclination angle to 0.

FIG. 19. As Figure 18 but now for component masses (50M$_\odot$, 10M$_\odot$).

[1] The LIGO Scientific Collaboration, J. Aasi, *et al.*, Classical and Quantum Gravity **32**, 074001 (2015), arXiv:1411.4547 [gr-qc].

[2] B. P. Abbott, R. Abbott, T. D. Abbott, M. R. Abernathy, F. Acernese, K. Ackley, C. Adams, T. Adams, P. Addesso, R. X. Adhikari, and et al., Physical Review Letters **116**, 131103 (2016), arXiv:1602.03838 [gr-qc].

[3] F. Acernese *et al.*, Classical and Quantum Gravity **32**, 024001 (2015), arXiv:1408.3978 [gr-qc].

[4] B. P. Abbott *et al.* (LIGO Scientific, Virgo), Phys. Rev. X**9**, 031040 (2019), arXiv:1811.12907 [astro-ph.HE].

[5] B. Abbott *et al.* (LIGO Scientific, Virgo), Astrophys. J. Lett. **892**, L3 (2020), arXiv:2001.01761 [astro-ph.HE].

[6] R. Abbott *et al.* (LIGO Scientific, Virgo), (2020), arXiv:2004.08342 [astro-ph.HE].

[7] K. Belczynski, A. Buonanno, M. Cantiello, C. L. Fryer, D. E. Holz, I. Mandel, M. C. Miller, and M. Walczak, Astrophys. J. **789**, 120 (2014), arXiv:1403.0677 [astro-ph.HE].

[8] K. Belczynski, D. E. Holz, T. Bulik, and R. O'Shaughnessy, Nature **534**, 512 (2016), arXiv:1602.04531 [astro-ph.HE].

[9] S. Stevenson, A. Vigna-Gómez, I. Mandel, J. W. Barrett, C. J. Neijssel, D. Perkins, and S. E. de Mink, Nature Communications **8**, 14906 (2017), arXiv:1704.01352 [astro-ph.HE].

[10] S. E. de Mink and I. Mandel, MNRAS **460**, 3545 (2016), arXiv:1603.02291 [astro-ph.HE].

[11] C. J. Hailey *et al.*, Nature **556** (2018), 10.1038/nature25029.

[12] A. C. Sippel and J. R. Hurley, MNRAS **430**, L30 (2013), arXiv:1211.6608 [astro-ph.GA].

[13] J. Strader, L. Chomiuk, T. J. Maccarone, J. C. A. Miller-Jones, and A. C. Seth, Nature (London) **490**, 71 (2012), arXiv:1210.0901 [astro-ph.HE].

[14] J. Samsing, D. J. D'Orazio, A. Askar, and M. Giersz, ArXiv e-prints (2018), arXiv:1802.08654 [astro-ph.HE].

[15] J. Samsing and E. Ramirez-Ruiz, Astrophys. J. Lett **840**, L14 (2017), arXiv:1703.09703 [astro-ph.HE].

[16] J. Samsing, M. MacLeod, and E. Ramirez-Ruiz, Astrophys. J. **784**, 71 (2014), arXiv:1308.2964 [astro-ph.HE].

[17] J. Samsing, Phys. Rev. D **97**, 103014 (2018), arXiv:1711.07452 [astro-ph.HE].

[18] N. W. C. Leigh, A. M. Geller, B. McKernan, K. E. S. Ford, M. M. Mac Low, J. Bellovary, Z. Haiman, W. Lyra, J. Samsing, M. O'Dowd, B. Kocsis, and S. Endlich, MNRAS **474**, 5672 (2018), arXiv:1711.10494 [astro-ph.GA].

[19] J. Samsing, A. Askar, and M. Giersz, Astrophys. J. **855**, 124 (2018), arXiv:1712.06186 [astro-ph.HE].

[20] J. Samsing, M. MacLeod, and E. Ramirez-Ruiz, Astrophys. J. **853**, 140 (2018), arXiv:1706.03776 [astro-ph.HE].

[21] L. Randall and Z.-Z. Xianyu, Astrophys. J. **853**, 93 (2018), arXiv:1708.08569 [gr-qc].

[22] E. A. Huerta and J. R. Gair, Phys. Rev. D **79**, 084021 (2009), arXiv:0812.4208.

[23] J. Samsing, M. MacLeod, and E. Ramirez-Ruiz, Astrophys. J. **846**, 36 (2017), arXiv:1609.09114 [astro-ph.HE].

[24] J. Samsing and T. Ilan, MNRAS **476**, 1548 (2018), arXiv:1706.04672 [astro-ph.HE].

[25] E. A. Huerta, S. T. McWilliams, J. R. Gair, and S. R. Taylor, Phys. Rev. D **92**, 063010 (2015), arXiv:1504.00928 [gr-qc].

[26] J. Samsing and T. Ilan, MNRAS **482**, 30 (2019), arXiv:1709.01660 [astro-ph.HE].

[27] J. Samsing, N. W. C. Leigh, and A. A. Trani, MNRAS **481**, 5436 (2018), arXiv:1803.08215 [astro-ph.HE].

[28] E. A. Huerta, P. Kumar, S. T. McWilliams, R. O'Shaughnessy, and N. Yunes, Phys. Rev. D **90**, 084016 (2014), arXiv:1408.3406 [gr-qc].

[29] F. Antonini, N. Murray, and S. Mikkola, Astrophys. J. **781**, 45 (2014), arXiv:1308.3674 [astro-ph.HE].

[30] J. Samsing and D. J. D'Orazio, MNRAS **481**, 5445 (2018), arXiv:1804.06519 [astro-ph.HE].

[31] D. J. D'Orazio and J. Samsing, MNRAS **481**, 4775 (2018), arXiv:1805.06194 [astro-ph.HE].

[32] J. Samsing and D. J. D'Orazio, arXiv e-prints , arXiv:1807.08864 (2018), arXiv:1807.08864 [astro-ph.HE].

[33] M. Zevin, J. Samsing, C. Rodriguez, C.-J. Haster, and E. Ramirez-Ruiz, arXiv e-prints , arXiv:1810.00901 (2018), arXiv:1810.00901 [astro-ph.HE].

[34] C. L. Rodriguez, P. Amaro-Seoane, S. Chatterjee, K. Kremer, F. A. Rasio, J. Samsing, C. S. Ye, and M. Zevin, Phys. Rev. D **98**, 123005 (2018), arXiv:1811.04926 [astro-ph.HE].

[35] K. Kremer, C. L. Rodriguez, P. Amaro-Seoane, K. Breivik, S. Chatterjee, M. L. Katz, S. L. Larson, F. A. Rasio, J. Samsing, C. S. Ye, and M. Zevin, arXiv e-prints , arXiv:1811.11812 (2018), arXiv:1811.11812 [astro-ph.HE].

[36] J. Lopez, Martin, A. Batta, E. Ramirez-Ruiz, I. Martinez, and J. Samsing, arXiv e-prints , arXiv:1812.01118 (2018), arXiv:1812.01118 [astro-ph.HE].

[37] B.-M. Hoang, S. Naoz, B. Kocsis, F. A. Rasio, and F. Dosopoulou, Astrophys. J. **856**, 140 (2018), arXiv:1706.09896 [astro-ph.HE].

[38] L. Gondán, B. Kocsis, P. Raffai, and Z. Frei, Astrophys. J. **855**, 34 (2018), arXiv:1705.10781 [astro-ph.HE].

[39] B.-M. Hoang, S. Naoz, B. Kocsis, F. A. Rasio, and F. Dosopoulou, Astrophys. J. **856**, 140 (2018), arXiv:1706.09896 [astro-ph.HE].

[40] L. Randall and Z.-Z. Xianyu, ArXiv e-prints (2018), arXiv:1802.05718 [gr-qc].

[41] B. Mikóczi, B. Kocsis, P. Forgács, and M. Vasúth, Phys. Rev. D **86**, 104027 (2012), arXiv:1206.5786 [gr-qc].

[42] S. Naoz, B. Kocsis, A. Loeb, and N. Yunes, Astrophys. J. **773**, 187 (2013), arXiv:1206.4316 [astro-ph.SR].

[43] L. Gondán and B. Kocsis, arXiv e-prints , arXiv:1809.00672 (2018), arXiv:1809.00672 [astro-ph.HE].

[44] F. Antonini and F. A. Rasio, Astrophys. J. **831**, 187 (2016), arXiv:1606.04889 [astro-ph.HE].

[45] E. A. Huerta and D. A. Brown, Phys. Rev. D **87**, 127501 (2013), arXiv:1301.1895 [gr-qc].

[46] M. Arca-Sedda, G. Li, and B. Kocsis, arXiv e-prints , arXiv:1805.06458 (2018), arXiv:1805.06458 [astro-ph.HE].

[47] Á. Takács and B. Kocsis, Astrophys. J. **856**, 113 (2018), arXiv:1712.04449 [astro-ph.GA].

[48] L. Gondán, B. Kocsis, P. Raffai, and Z. Frei, Astrophys. J. **860**, 5 (2018), arXiv:1711.09989 [astro-ph.HE].

[49] F. Antonini, M. Gieles, and A. Gualandris, arXiv e-prints , arXiv:1811.03640 (2018), arXiv:1811.03640 [astro-ph.HE].

[50] F. Antonini, S. Chatterjee, C. L. Rodriguez, M. Morscher, B. Pattabiraman, V. Kalogera, and F. A. Rasio, Astrophys. J. **816**, 65 (2016), arXiv:1509.05080.

[51] B. Abbott et al. (LIGO Scientific, Virgo), Astrophys. J. **883**, 149 (2019), arXiv:1907.09384 [astro-ph.HE].

[52] A. H. Nitz, A. Lenon, and D. A. Brown, The Astrophysical Journal **890**, 1 (2020).

[53] M. E. Lower, E. Thrane, P. D. Lasky, and R. Smith, Phys. Rev. D **98**, 083028 (2018), arXiv:1806.05350 [astro-ph.HE].

[54] I. Hinder, F. Herrmann, P. Laguna, and D. Shoemaker, Phys. Rev. D **82**, 024033 (2010).

[55] S. Tiwari, G. Achamveedu, M. Haney, and P. Hemantakumar, Phys. Rev. D **99**, 124008 (2019), arXiv:1905.07956 [gr-qc].

[56] M. Ebersold, Y. Boetzel, G. Faye, C. K. Mishra, B. R. Iyer, and P. Jetzer, Phys. Rev. D **100**, 084043 (2019), arXiv:1906.06263 [gr-qc].

[57] Y. Boetzel, C. K. Mishra, G. Faye, A. Gopakumar, and B. R. Iyer, Phys. Rev. D **100**, 044018 (2019), arXiv:1904.11814 [gr-qc].

[58] B. Ireland, O. Birnholtz, H. Nakano, E. West, and M. Campanelli, Phys. Rev. D **100**, 024015 (2019), arXiv:1904.03443 [gr-qc].

[59] B. Moore and N. Yunes, Class. Quant. Grav. **36**, 185003 (2019), arXiv:1903.05203 [gr-qc].

[60] N. Loutrel, S. Liebersbach, N. Yunes, and N. Cornish, Class. Quant. Grav. **36**, 025004 (2019), arXiv:1810.03521 [gr-qc].

[61] N. Loutrel and N. Yunes, Classical and Quantum Gravity **34**, 044003 (2017), arXiv:1607.05409 [gr-qc].

[62] E. A. Huerta, C. J. Moore, P. Kumar, D. George, A. J. K. Chua, R. Haas, E. Wessel, D. Johnson, D. Glennon, A. Rebei, A. M. Holgado, J. R. Gair, and H. P. Pfeiffer, Phys. Rev. D **97**, 024031 (2018), arXiv:1711.06276 [gr-qc].

[63] E. A. Huerta, P. Kumar, B. Agarwal, D. George, H.-Y. Schive, H. P. Pfeiffer, R. Haas, W. Ren, T. Chu, M. Boyle, D. A. Hemberger, L. E. Kidder, M. A. Scheel, and B. Szilagyi, Phys. Rev. D **95**, 024038 (2017), arXiv:1609.05933 [gr-qc].

[64] I. Hinder, L. E. Kidder, and H. P. Pfeiffer, Phys. Rev. D **98**, 044015 (2018), arXiv:1709.02007 [gr-qc].

[65] Z. Cao and W.-B. Han, Phys. Rev. D **96**, 044028 (2017), arXiv:1708.00166 [gr-qc].

[66] T. Hinderer and S. Babak, Phys. Rev. D **96**, 104048 (2017), arXiv:1707.08426 [gr-qc].

[67] X. Liu, Z. Cao, and L. Shao, Phys. Rev. D **101**, 044049 (2020), arXiv:1910.00784 [gr-qc].

[68] D. Chiaramello and A. Nagar, (2020), arXiv:2001.11736 [gr-qc].

[69] E. A. Huerta, R. Haas, S. Habib, A. Gupta, A. Rebei, V. Chavva, D. Johnson, S. Rosofsky, E. Wessel, B. Agarwal, D. Luo, and W. Ren, Phys. Rev. D **100**, 064003 (2019), arXiv:1901.07038 [gr-qc].

[70] I. Hinder, L. E. Kidder, and H. P. Pfeiffer, ArXiv e-prints (2017), arXiv:1709.02007 [gr-qc].

[71] S. Habib and E. Huerta, Phys. Rev. D **100**, 044016 (2019), arXiv:1904.09295 [gr-qc].

[72] D. Johnson, E. A. Huerta, and R. Haas, Classical and Quantum Gravity **35**, 027002 (2018), arXiv:1708.02941 [gr-qc].

[73] A. Ramos-Buades, S. Husa, G. Pratten, H. Estellés, C. García-Quirós, M. Mateu-Lucena, M. Colleoni, and R. Jaume, Phys. Rev. D **101**, 083015 (2020), arXiv:1909.11011 [gr-qc].

[74] A. Rebei, E. A. Huerta, S. Wang, S. Habib, R. Haas, D. Johnson, and D. George, Phys. Rev. D **100**, 044025 (2019), arXiv:1807.09787 [gr-qc].

[75] I. M. Romero-Shaw, P. D. Lasky, and E. Thrane, MNRAS **490**, 5210 (2019), arXiv:1909.05466 [astro-ph.HE].

[76] V. Tiwari, S. Klimenko, N. Christensen, E. A. Huerta, S. R. P. Mohapatra, A. Gopakumar, M. Haney, P. Ajith, S. T. McWilliams, G. Vedovato, M. Drago, F. Salemi, G. A. Prodi, C. Lazzaro, S. Tiwari, G. Mitselmakher, and F. Da Silva, Phys. Rev. D **93**, 043007 (2016), arXiv:1511.09240 [gr-qc].

[77] A. Ramos-Buades, S. Tiwari, M. Haney, and S. Husa, Phys. Rev. D **102**, 043005 (2020), arXiv:2005.14016 [gr-qc].

[78] S. Wu, Z. Cao, and Z.-H. Zhu, MNRAS **495**, 466 (2020), arXiv:2002.05528 [astro-ph.IM].

[79] I. M. Romero-Shaw, N. Farrow, S. Stevenson, E. Thrane, and X.-J. Zhu, MNRAS **496**, L64 (2020), arXiv:2001.06492 [astro-ph.HE].

[80] K. G. Arun, L. Blanchet, B. R. Iyer, and S. Sinha, Phys. Rev. D **80**, 124018 (2009), arXiv:0908.3854 [gr-qc].

[81] K. G. Arun, L. Blanchet, B. R. Iyer, and M. S. S. Qusailah, Phys. Rev. D **77**, 064034 (2008), arXiv:0711.0250 [gr-qc].

[82] L. Blanchet, Living Reviews in Relativity **9**, 4 (2006).

[83] S. Habib and E. A. Huerta, Phys. Rev. D **100**, 044016 (2019), arXiv:1904.09295 [gr-qc].

[84] C. E. Rasmussen and C. K. I. Williams, Gaussian Processes for Machine Learning (Adaptive Computation and Machine Learning) (The MIT Press, 2005).

[85] M. Boyle et al., Class. Quant. Grav. **36**, 195006 (2019), arXiv:1904.04831 [gr-qc].

[86] A. Bohé, L. Shao, A. Taracchini, A. Buonanno, S. Babak, I. W. Harry, I. Hinder, S. Ossokine, M. Pürrer, V. Raymond, T. Chu, H. Fong, P. Kumar, H. P. Pfeiffer, M. Boyle, D. A. Hemberger, L. E. Kidder, G. Lovelace, M. A. Scheel, and B. Szilágyi, Phys. Rev. D **95**, 044028 (2017), arXiv:1611.03703 [gr-qc].

[87] L. Barsotti, P. Fritschel, M. Evans, and S. Gras, "Updated Advanced LIGO sensitivity design curves," (2018), https://dcc.ligo.org/LIGO-T1800044/public.

[88] LIGO Scientific Collaboration, "LIGO Algorithm Library - LALSuite," free software (GPL) (2018).

[89] L. S. Finn, Phys. Rev. D **63**, 102001 (2001), gr-qc/0010033.

[90] B. F. Schutz, Classical and Quantum Gravity **28**, 125023 (2011), arXiv:1102.5421 [astro-ph.IM].

[91] M. Evans, R. Sturani, S. Vitale, and E. Hall, "Sensitivity Curves for advanced Virgo, Kagra, Cosmic Explorer and the Einstein Telescope," (2018), https://dcc.ligo.org/LIGO-T1500293-v11/public.

[92] D. Reitze, R. X. Adhikari, S. Ballmer, B. Barish, L. Barsotti, G. Billingsley, D. A. Brown, Y. Chen, D. Coyne, R. Eisenstein, M. Evans, P. Fritschel, E. D. Hall, A. Lazzarini, G. Lovelace, J. Read, B. S. Sathyaprakash, D. Shoemaker, J. Smith, C. Torrie, S. Vitale, R. Weiss, C. Wipf, and M. Zucker, "Cosmic explorer: The u.s. contribution to gravitational-wave astronomy beyond ligo," (2019), arXiv:1907.04833 [astro-ph.IM].

[93] M. Punturo *et al.*, Class. Quant. Grav. **27**, 194002 (2010).

[94] F. Amann, F. Bonsignorio, T. Bulik, H. J. Bulten, S. Cuccuru, A. Dassargues, R. DeSalvo, E. Fenyvesi, F. Fidecaro, I. Fiori, C. Giunchi, A. Grado, J. Harms, S. Koley, L. Kovacs, G. Losurdo, V. Mandic, P. Meyers, L. Naticchioni, F. Nguyen, G. Oggiano, M. Olivieri, F. Paoletti, A. Paoli, W. Plastino, M. Razzano, P. Ruggi, G. Saccorotti, A. M. Sintes, L. Somlai, P. Van, and M. Vasuth, "Site-selection criteria for the einstein telescope," (2020), arXiv:2003.03434 [physics.ins-det].

[95] Cosmic Explorer, https://cosmicexplorer.org/.

[96] M. Maggiore, C. Van Den Broeck, N. Bartolo, E. Belgacem, D. Bertacca, M. A. Bizouard, M. Branchesi, S. Clesse, S. Foffa, J. García-Bellido, S. Grimm, J. Harms, T. Hinderer, S. Matarrese, C. Palomba, M. Peloso, A. Ricciardone, and M. Sakellariadou, Journal of Cosmology and Astroparticle Physics **2020**, 050 (2020), arXiv:1912.02622 [astro-ph.CO].

[97] Einstein Telescope, http://www.et-gw.eu/.

[98] A. K. Lenon, A. H. Nitz, and D. A. Brown, "Measuring the eccentricity of gw170817 and gw190425," (2020), arXiv:2005.14146 [astro-ph.HE].

[99] NCSA, "Illinois Campus Cluster Program," (2018), https://campuscluster.illinois.edu/.